

Abstract

Capture efficiencies of particles impacting on a circular cylinder in cross flow are presented. To understand the effect of turbulence on particle deposition, simulations of particle-laden flows at $Re_c = 420$ were performed. A high order direct numerical simulation (DNS) code, The Pencil Code, has been used. A Lagrangian tracker solved the particle motions using the drag force. The cylinder boundary was resolved using the immersed boundary method. Capture efficiencies for the cylinder was found for different particle Stokes numbers (sizes), comparing laminar and turbulent inflows. Turbulence was created by isotropic forcing in two presimulations, with forcing at two different scales; large scale and medium scale. Turbulent inflow was simulated by imposing the velocity field of the presimulations on top of a mean flow velocity at the inlet. Turbulent inflows increased the front side capture efficiency, η_{front} , for particles in the range $0.15 < St < 0.40$. It has been showed that particles with an increased streamwise velocity have a higher probability of penetrating the boundary layer. The turbulent effects on η_{front} were strongest in the region where the sensitivity of η_{front} to a change in Stokes number is largest.

Preface

Background for master thesis

This report is written as a part of my degree in Master of Science and Technology (sivilingeniør) at the Norwegian University of Science and Technology (NTNU). The master thesis covers 30 credit units (studiepoeng), which is one semester. The work has consisted of reading relevant literature, producing and evaluating results as well as writing this report. The master thesis is a continuation of the work I did in the project thesis (15 credit units) last semester. The experience and lessons learned I got from the project thesis gave me a head start when starting working on the master thesis. All aspects discussed in the project thesis are also covered here. Therefore, this report can be considered as a more extensive, improved edition of the project report.

Acknowledgements

I would like to thank my supervisor, Nils Erland L. Haugen, for good support throughout this work. Haugen is an employee at SINTEF Energy, Department of Energy Processes, and through meetings twice a week and a ton of e-mails, he has been very forthcoming and helpful.

I would also like to thank Solveig Søvik Alnes and Ingeborg Monge Christoffersen, who have been working on similar projects, for inspirational discussions and invaluable help.

At the Department of Physics, I would like to thank my internal supervisor Jon Andreas Støvneng.

Contents

1	Introduction and background	9
1.1	Background	9
1.2	Turbulent flow	10
1.3	Cylinder in cross flow	12
1.4	Existing literature	13
2	Governing equation	14
2.1	The fluid equations	14
2.2	The particle equations	15
2.2.1	The particle drag force	15
3	Method of solution	18
3.1	Numerical methods	18
3.2	The Pencil Code	19
3.3	Length and time scales	20
3.4	Initial and boundary conditions	21
3.4.1	Creating turbulence by forcing	21
3.4.2	Flow around cylinder	24
3.4.3	The particles	25
3.5	Capture efficiency	26
3.6	Two dimensional turbulence	26
4	Parameter determination	28
4.1	Sound speed	28
4.2	Particle insertion	32
5	Results and discussion	34
5.1	Definition of cases	34
5.2	Validation of laminar simulations in 2D	34
5.3	Validation of grid resolution	36
5.4	Results with turbulent inflow	37
5.5	Comparison with experimental results	41
5.6	Turbulent inflow simulated in two dimensions	44

5.7	Discussion	45
5.7.1	Possible sources of error	52
5.7.2	Further issues	52
A	Parameters used in the Pencil Code	54
	Bibliography	55

List of Figures

1.1	Schematic drawing of biomass combustion	10
1.2	Photo of turbulent flow in water	11
1.3	Vorticity snapshots of cylinder flow	12
3.1	Overview of computational domains	21
3.2	Energy spectrum normalized with k_0	22
3.3	Relative Stokes number, St_E/St , as a function of wavenumber.	23
3.4	ω_z snapshots of turbulent inflow	25
3.5	Sketch explaining capture efficiency formula	26
4.1	Power spectra for different sound speeds	30
4.2	Power spectra for different inflows	31
4.3	Particle insertion parameters	33
5.1	Laminar inflow simulations in 2D and 3D	35
5.2	Capture efficiency for high resolution simulation	36
5.3	Capture efficiencies for turbulent inflow	38
5.4	Cylinder angle explained	39
5.5	Deposition density distributions, $n(\theta)$	40
5.6	Average time spent in fluid before deposition	42
5.7	Capture efficiencies from experimental results	43
5.8	Capture efficiencies for turbulence simulated in 2D	46
5.9	z vorticity for laminar and $k_n = 1.5$	47
5.10	z vorticity for laminar and $k_n = 1.5$, cylinder zoom	48
5.11	Relative differences in capture efficiency, including effective Stokes numbers	50

List of Tables

4.1	Magnitudes of length parameters in units of L_{yz}	32
5.1	Back side capture efficiency for $St = 0.1$	35
5.2	Capture efficiencies comparing laminar and $k_n = 1.5$	49

Chapter 1

Introduction and background

1.1 Background

The main motivation for studying particle deposition is the fact that it has many engineering applications. Often a small amount of matter in solid state is carried along with a fluid flow. A typical example is the presence of dust in indoor air. The dust can be deposited on solid surfaces. This phenomenon is easily seen inside fan cooled electronics, e.g. on the inside of a computer cabinet, where a layer of dust will form.

An industrial segment where particle deposition is of great significance, is boiler and combustion facilities. In biomass combustion facilities, for example, biomass is combusted and the heat from this process is utilized through heat exchangers. The heat exchangers transfer heat energy from a hot gas flow to a working fluid, see figure 1.1 for a schematic drawing. The hot gas will typically contain ash particles from the combustion process. The design of the heat exchangers may vary, but in a typical setup, the working fluid is sent through cylinders across the flow. Obviously, in a facility like this, one wants to maximize the thermal energy transfer. From experience, a layer of particles around a heat exchanging cylinder will have an insulating effect and lower the heat exchange rate. This causes problems in terms of loss of efficiency and maintenance costs. Thus, in this type of facility, it is desired to minimize particle deposition.

Several deposition mechanisms can be studied. Vapors can condensate to or chemically react with a solid surface. For small particles (sub micrometer scale), Brownian diffusion and thermophoresis (particle motion due to a local temperature gradient) can play a role. Gravity will affect the particles, and increase deposition especially on horizontal surfaces. This work will, however, only focus on the effect of inertial impaction. When a particle actually touches the solid surface, it is assumed to be deposited. This is probably a good assumption for sticky ash particles in a hot gas flow, but definitely not for all cases. Sand particles carried in a water flow, for example, have little to no probability of deposition to a solid object. However, the results will have a general appeal, since they will show how many particles will touch the cylinder surface. For cases where there is no probability of deposition, the touching particles may lead to erosion of the cylinder. See e.g. Fan et al. [20] for a study of erosion due to particle impaction.

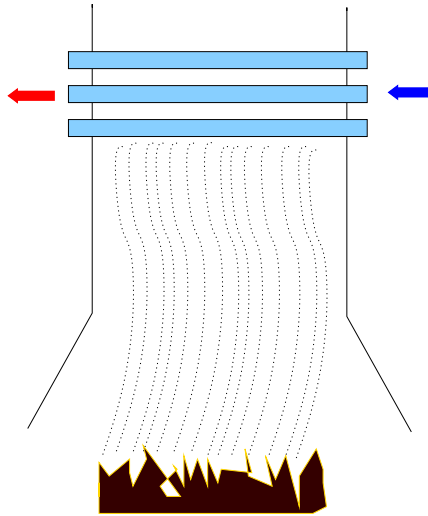


Figure 1.1: Schematic drawing of biomass combustion. Heat from a gas flow containing particles, is exchanged to a working fluid (typically water) in a heat exchanger. The heated working fluid can be used for district heating of buildings or to produce electricity. Particle deposition on the heat exchanger will cause problems in terms of loss of efficiency and maintenance costs.

The main objective of this project is to study the effect of turbulence on the particle deposition. Capture efficiencies for turbulent flows are compared with results from laminar flows. Results have been produced by numerical simulations. Chapter 2 describes the equations that need to be solved for the fluid and the particles. Chapter 3 explains the methods and approaches used in this work, chapter 4 discusses choice of different parameters used, while chapter 5 presents and discusses the results.

1.2 Turbulent flow

Turbulent flows can easily be observed in our daily life. The smoke coming out of a chimney and the water in a rocky river have characteristics we call turbulent. Turbulence is irregular and seemingly random and chaotic. Mathematically, we can say that the velocity field of a turbulent flow, $\mathbf{u}(\mathbf{x}, t)$, varies significantly in both position and time. A large span of length and time scales is present. This can be seen in figure 1.2. Turbulence is three dimensional by nature. Even if turbulence is produced by two dimensional geometry, turbulent eddies will evolve in all three dimensions. Turbulent flows are also dissipative, meaning that kinetic energy is lost to other energy forms such as heat and sound. This means that turbulence needs a source of energy to be maintained.

When describing turbulence, one often looks at statistical averages instead of instantaneous values. Furthermore, it is useful to look at fluctuating quantities, where the mean values have been subtracted from the instantaneous values. This work follows the notation

$$\mathbf{u} = \mathbf{U} + \mathbf{u}'$$



Figure 1.2: A photo of water flow in the Niagara River. We can see that the largest turbulent eddies span about half the image. But we can also see smaller eddies. All the way down to the pixel size of the image we can distinguish turbulent structures. It is apparent that in this flow, a large span of length scales is present. (Photo and copyright by Mark Visosky)

where \mathbf{u} is the instantaneous velocity, \mathbf{U} is the mean flow velocity and \mathbf{u}' is the fluctuating velocity. It is important to emphasize that these are velocity values for each point in space. We are, however, sometimes only interested in the overall mean flow in the whole domain. This is referred to as \mathbf{U}_o , given by

$$\mathbf{U}_o = \frac{1}{V} \int_V \mathbf{U} d\mathbf{x},$$

where V is the volume of the domain. Similarly, we can express the fluctuating velocities in terms of their root mean square value for the whole domain, giving an indication of the overall turbulent intensity. The root mean square velocity of the fluctuations is defined as

$$u_{\text{rms}} = \sqrt{\frac{1}{V} \int_V u'^2 d\mathbf{x}}.$$

In laminar flows, which are highly ordered and the mean flow equals the instantaneous flow, one often describes the flow with the velocity field, $\mathbf{u}(\mathbf{x}, t)$. This can be done with turbulent flows too, but since turbulence consists of rotational structures, one can also describe turbulent flows with the *vorticity* field, $\boldsymbol{\omega}(\mathbf{x}, t)$. For visualization purposes, the vorticity is a useful quantity to plot. The vorticity field is the curl of the velocity field

$$\boldsymbol{\omega} = \nabla \times \mathbf{u}.$$

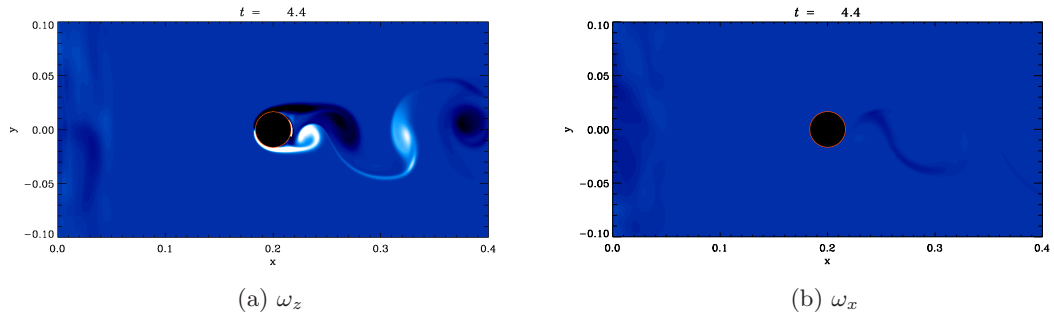


Figure 1.3: Snapshots of vorticity at Reynolds number $Re_c = 420$. Fig. (a) shows vorticity in the spanwise (z) direction, ω_z , while fig. (b) shows vorticity in the streamwise (x) direction, ω_x . At this Reynolds number, the vortex street has a three dimensional nature.

1.3 Cylinder in cross flow

Flow dynamics in the flow around a circular cylinder has been subject to extensive research for several decades. Its importance in engineering applications is clearly a driving factor. But also the simplicity of the setup may be tempting for laboratory and computational experiments. The flow around a cylinder can be divided into three components: a boundary layer, a separating free shear layer and a wake. Vortices, rotational structures in the flow, are produced in the cylinder wake, but, as pointed out by Williamson (1996, [13]), the behaviour of these vortices is strongly dependent on the Reynolds number. The Reynolds number for a flow around a cylinder is given by

$$Re_c = \frac{d_c U_0}{\nu}, \quad (1.1)$$

where d_c is cylinder diameter, U_0 is the mean flow velocity and ν is the kinematic viscosity of the fluid. In the wake of the cylinder, vortices of opposite direction of rotation are formed. For sufficiently large Reynolds numbers, these will be shed from the cylinder and form what is called a vortex street downstream from the cylinder. See figure 1.3 for snapshots of the vortex street. Williamson (1996, [13]) defines the following vortex shedding regimes:

- **Laminar steady regime** ($Re_c < 49$)
In this regime, a steady recirculation region of two symmetrically placed vortices is formed.
- **Laminar vortex shedding regime** ($Re_c \sim 49$ to 190)
Vortices will no longer form a steady recirculation region, but will develop instabilities. A vortex street will be formed, which is purely periodic and two-dimensional.
- **3D wake transition regime** ($Re_c \sim 190$ to 260)
A transition regime with a gradually increasing influence from 3D effects. Sudden discontinuities in vortex behaviour exist in this regime.

- **3D regimes** ($Re_c > 260$)

In the lower end of this region, with Re_c less than about 1000, a very similar state to the laminar vortex shedding regime exists, with the exception of the presence of fine-scale streamwise vortex structures. Williamson (1996, [13]) further describes flow behaviour for $Re_c > 1000$, but this is not relevant in this work.

1.4 Existing literature

Particle deposition in boiler type power plants has always been an issue. Traditionally, fossil fuels like coal or natural gas have been used. But biomass fuels are gaining popularity, and, as Zhou et. al. [10] show, they severely increase deposit problems. The nature behind and mechanisms of the biomass deposits have thus been subject to recent research. Zhou et. al. [10] and Srikanth et. al. [22] are examples of this. They show that it is the large quantities of alkali in many types of biomass that will easily deposit on solid surfaces. They also show that for relatively large particles, with diameters larger than 10 μm , inertial impaction is the most important deposition mechanism.

Rosner & Tandon [6] and Wang [3] are examples of studies that focus on particle deposition on a cylinder. Their focus is, however, on the sticking probability of the particles. Wang presents a theoretical study on sticking efficiency, and Rosner & Tandon explain how sticking depends on velocity magnitude and direction, and how the deposit layer will grow. The results they present are important for understanding particle deposition on a cylinder, but are not directly relevant for this work. A perfect (100%) sticking efficiency is assumed in this project. In more applied, single case studies sticking probability would be important to take into account. Haugen & Kragset [15] presents a recent article discussing particle deposition on a cylinder in laminar flow. The conclusions they make, will be discussed in relation to turbulent flow in this report.

Douglas & Ilias [14] have experimentally found capture efficiencies for a cylinder in turbulent cross flow. The results they present will be compared with results found from simulations in this work. The range of Reynold's numbers in the article are, however, larger than in this work. Besides Douglas & Ilias, no literature have been found on cylinder deposition in turbulent cross flow.

Chapter 2

Governing equation

Five fundamental equations are solved in this project, three for the fluid and two for the particles.

2.1 The fluid equations

The essential equations that need to be solved are the continuity equation

$$\frac{\partial \rho}{\partial t} + \nabla \cdot (\rho \mathbf{u}) = 0, \quad (2.1)$$

and the Navier-Stokes equation

$$\frac{\partial \mathbf{u}}{\partial t} + \mathbf{u} \cdot \nabla \mathbf{u} = -\frac{1}{\rho} \nabla P + \frac{1}{\rho} \nabla \cdot \boldsymbol{\tau} + \frac{\mathbf{F}}{\rho}, \quad (2.2)$$

where ρ is the fluid density, \mathbf{u} is the velocity, P is the pressure, $\boldsymbol{\tau} = 2\rho\nu\mathbf{S}$ is the stress tensor, $\mathbf{S} = \frac{1}{2}(\nabla\mathbf{u} + (\nabla\mathbf{u})^T) - \frac{1}{3}\mathbb{I}_3\nabla\cdot\mathbf{u}$ is the traceless rate of strain tensor, \mathbb{I}_3 is the three by three identity matrix and ν is the kinematic viscosity. \mathbf{F} is the sum of all body forces acting on the fluid, e.g. gravity. When inserting particles in the flow, the particles can have an influence on the fluid through a force \mathbf{F}_{p-f} . This force is, however, neglected, because relatively few particles are inserted, and their sizes are small compared to the dominant flow structures. The set of equation (2.1) and (2.2) are often referred to as the Navier-Stokes equations.

Compressible flow is considered. Thus an isothermal equation of state is used to obtain closure of the PDEs, i.e.

$$P = \rho c^2, \quad (2.3)$$

where c is the speed of sound. Now, the five unknown variables (P , ρ and three velocity components u_i) can be found from the five equations ((2.1), (2.3) and three components of (2.2)).

2.2 The particle equations

While the fluid equations are solved in an Eulerian formalism, the particle equations are solved in the Lagrangian formalism. This means that the fluid equations are solved at fixed grid points in our domain, while the particles are tracked individually from time step to time step. The particle equations consist of the equation for particle position, \mathbf{x} ,

$$\frac{d\mathbf{x}}{dt} = \mathbf{v}, \quad (2.4)$$

and the equation for particle velocity, \mathbf{v} ,

$$\frac{d\mathbf{v}}{dt} = \frac{1}{m_p} \sum \mathbf{F}_i, \quad (2.5)$$

where m_p is particle mass and $\sum \mathbf{F}_i$ is the sum of all the forces acting on the particle. Relevant particle forces include the drag force \mathbf{F}_D , the gravity force \mathbf{F}_g , the lift force \mathbf{F}_L , the inter particle force \mathbf{F}_{p-p} , the thermophoretic force \mathbf{F}_T , the force due to Brownian motions \mathbf{F}_B and the particle wall force \mathbf{F}_W . To make a completely realistic simulation, all these forces would have to be accounted for. Particles touching the wall are assumed to be deposited and are removed from the simulation, thus the particle wall force, \mathbf{F}_W , is not relevant to include. The particles inserted are small enough that the gravity force, \mathbf{F}_g , can safely be disregarded. The particle drag force, \mathbf{F}_D , will be discussed in the next section. Implementation of the other relevant forces is beyond the scope of this project.

2.2.1 The particle drag force

Particles are assumed to have spherical shape. According to Crowe et. al. (Chapter 4, [2]), the drag force is given by

$$\mathbf{F}_D = \frac{1}{2} \rho C_D A |\mathbf{u} - \mathbf{v}| (\mathbf{u} - \mathbf{v}) / C_c, \quad (2.6)$$

where ρ is the density of the fluid, and $A = \pi r_p^2$ is the cross sectional area of the particle, r_p is particle radius, \mathbf{u} is the velocity of the fluid, \mathbf{v} is the velocity of the particle,

$$C_c = 1 + \frac{\lambda}{r_p} \left(1.257 + 0.4e^{(-1.1r_p/\lambda)} \right) \quad (2.7)$$

is the Stokes-Cunningham factor, and λ is the mean free path for a typical molecule in the gas. The Stokes-Cunningham factor takes into account that for very small particles the surrounding medium is no longer a continuous fluid, but rather distinct molecules. The constants in C_c have been found empirically¹, and varies slightly in magnitude. The constants used in (2.7) are those found by Davies (1945, [4]).

¹An expression for the correction of the drag factor was first found by Millikan (1923) as a part of his oil drop experiment

Assuming air at room temperature, $\lambda = 67$ nm is a commonly used value. All particles studied in this work will be in the micrometer range, i.e. $\lambda/r_p \ll 1$. The quantity $\text{Kn} = \lambda/r_p$, is referred to as the Knudsen number. $\text{Kn} \ll 1$ is valid in the continuum regime, and in this regime the Stokes-Cunningham factor can be neglected [27]. Thus the results presented here will be general for particles in the continuum regime, but will not be correct when Kn approaches unity.

The drag coefficient is given by

$$C_D = \begin{cases} 0.44 & \text{for } \text{Re}_p > 1000 \\ \frac{24}{\text{Re}_p} (1 + 0.15\text{Re}_p^{0.687}) & \text{for } \text{Re}_p < 1000 \end{cases}, \quad (2.8)$$

where Re_p is the Reynolds number based on the particle diameter, d_p and the relative slip velocity between the particle and the fluid:

$$\text{Re}_p = \frac{d_p |\mathbf{v} - \mathbf{u}|}{\nu}. \quad (2.9)$$

With particle diameters in the micrometer range, kinematic viscosity around $\nu \simeq 10^{-4}$ m²/s and particle velocities similar to the fluid velocity, we can see that Re_p is lower than 1, and thus it is the second case of the drag coefficient, C_D , that is the relevant one. Furthermore, we see that the second term is negligible, i.e. $0.15\text{Re}_p^{0.687} \ll 1$ for $\text{Re}_p < 1$. Equation (2.8) can then be simplified to

$$C_D = \frac{24}{\text{Re}_p} = \frac{24\nu}{d_p |\mathbf{v} - \mathbf{u}|}. \quad (2.10)$$

The drag force, (2.6), then simplifies to

$$\mathbf{F}_D = m_p (\mathbf{u} - \mathbf{v}) \cdot \frac{12\rho\nu\pi (\frac{1}{2}d_p)^2}{m_p d_p C_c} = \frac{m_p}{\tau_p} (\mathbf{u} - \mathbf{v}), \quad (2.11)$$

where we have introduced the particle response time, τ_p ,

$$\tau_p = \frac{m_p d_p C_c}{12\rho\nu\pi (\frac{1}{2}d_p)^2} = \frac{\rho_p d_p^2}{18\rho\nu}. \quad (2.12)$$

A common way of describing particles in fluid flow, is by introducing the Stokes number. The Stokes number is defined as the particle response time, τ_p , divided by some characteristic time for the fluid, τ_f , i.e.

$$\text{St} = \frac{\tau_p}{\tau_f}. \quad (2.13)$$

The Stokes number tells us to what degree the particle motion is controlled by the particle's own inertia. Or, vice versa, to what degree the particle will follow the flow. For $\text{St} \gg 1$ the particles will move in straight lines and collide with solid bodies in the flow, whereas for $\text{St} \ll 1$ the particles will follow the streamlines. For a cylinder in a

cross flow, a characteristic time is $\tau_f = r_c/U_0$, where r_c is the radius of the cylinder, and U_0 is the mean flow velocity. Using (2.12), the Stokes number is expressed as

$$\text{St} = \frac{\rho_p d_p^2 U_0}{18 \rho \nu r_c}. \quad (2.14)$$

Using equations (2.5) and (2.11), we can simplify the equation for the particle velocity to

$$\frac{d\mathbf{v}}{dt} = \frac{U_0}{\text{St} \cdot r_c} (\mathbf{u} - \mathbf{v}). \quad (2.15)$$

We see that the acceleration of the particles has an inverse proportionality with the Stokes number. Large Stokes numbers will have lower acceleration, as expected.

Chapter 3

Method of solution

3.1 Numerical methods

Analytical solutions to turbulent flows do not exist, therefore a numerical method must be used to solve the equations. Different numerical approaches can be used. Regardless of the approach, a computational grid must be chosen. At each grid point, also called mesh point, the relevant equations are solved for the fluid. This process is repeated at every given time interval, referred to as the time step. The grid needs to be three dimensional, because of the three dimensional nature of turbulence.

Direct Numerical Simulations (DNS) solve the Navier-Stokes equations directly. The clear advantage of using DNS is that no simplifications or approximations are used when solving Navier-Stokes. For this reason, DNS is considered as reliable as real laboratory experiments, with the advantage of no instrumental and measurement errors. See e.g. Kim et. al. [11] for a comparison of DNS and lab results. But, DNS has one major drawback - it requires a huge amount of CPU time. Because of this, DNS studies are mostly done with super-computers. Due to the rapid development of computer hardware, the DNS possibilities improve year by year. But still, DNS is restricted to relatively low Reynolds numbers to keep mesh spacing and time steps acceptably large.

Reynolds-averaged Navier-Stokes (RANS) is another method used for studying turbulent flows. In RANS the Navier-Stokes equation is time-averaged, and modelling is included to achieve simplification and closure of the equations. Unlike DNS, where the instantaneous flow field is solved, RANS tries to find the statistical (mean) evolution of the flow. Many different RANS models exist, some of them are specialized for certain types of flow. Computational fluid dynamics (CFD) tools for industrial purposes are typically using RANS. RANS computations requires considerably less CPU time than DNS, but the result is always dependent on the correctness of the modelling used.

A third way of simulating turbulence is using Large Eddy Simulations (LES). LES is essentially the same as DNS, except that the grid is not fine enough to resolve all scales. Therefore, a sub grid scale model is used to model the turbulent structures smaller than the grid separation. The small scales have, to some extent, a universal character. They are isotropic and not affected by the flow geometry. Therefore, relatively simple models

can be used to represent the smaller scales [1]. The large scales, which are affected by flow geometry and are not universal, are computed explicitly. In terms of computational cost, LES lies between RANS and DNS.

In this work, DNS is used. The effect of turbulence on particle deposition on cylinders is not a well investigated subject. Usually, RANS results are verified by comparison with lab and/or DNS results. For mean flow characteristics around a cylinder, a LES would probably be sufficient, but since particle deposition is studied, the behaviour of the small scale turbulence close to the cylinder surface might be very important. By using DNS in this work, hopefully some general conclusions can be made. At later stages, with more specialized applications of the simulations, RANS and LES can be considered.

3.2 The Pencil Code

The simulations in this project was run with The Pencil Code [23]. The Pencil Code is a high-order MPI (Message Passing Interface) code, primarily designed to deal with weakly compressible turbulent flows. Initially, it was created for solving Magnetohydrodynamics (MHD) problems. MHD is the field which studies the dynamics of electrically conducting fluids (e.g. plasmas). But because of its modular nature, The Pencil Code can easily be modified for other applications. In this project, magnetic and electric forces are disabled, but modules for particle tracking and solid bodies (i.e. cylinder) are included.

As pointed out by Moin & Mahesh [19], spectral methods (solving the equations in Fourier space) are superior to spatial derivative schemes in terms of differentiation error. For this reason, spectral methods have weaker requirements to mesh spacing, and are commonly used in turbulence studies. The Pencil Code does, however, use a sixth order spatial derivative. This is mainly due to two reasons. Firstly, easier parallelization of spatial derivatives is of great importance. Secondly, spatial derivative schemes have more flexibility in boundary conditions, whereas the spectral methods are difficult to implement with non-periodic boundaries. In addition, finite difference schemes typically have lower levels of aliasing error than spectral methods. For time stepping, a third-order Runge-Kutta scheme is used. This choice is based on error minimization and memory usage arguments [23].

The Pencil Code is typically used with many CPUs working in parallel. The computational grid is split up evenly and one sub-domain is distributed to each CPU. In order to be CPU cache efficient, the equations are solved along one-dimensional arrays, “pencils”, hence the name Pencil Code. Since sixth order derivation is used, the code needs three grid points in each direction to do a derivative. Consequently, at each sub-domain boundary, data from three additional grid points must be aquired from the neighbouring CPU. A three grid point thick “ghost zone” layer along the domain boundary of each processor is therefore communicated between CPUs using MPI.

3.3 Length and time scales

In a DNS it is of vital importance that all scales are resolved. The smallest length and time scales are dictated by the physics, and we need to be sure that the grid point spacing and time steps are small enough to include these.

In turbulent flows a wide range of length scales are present. Length scales can typically be represented by the diameter of eddies. The largest scales are limited by the boundaries and solid objects in the flow. There is a cascade from big to smaller eddies, until at some minimum length scale the flow structures are destroyed by viscous forces. The Kolmogorov length scale

$$\eta = \left(\frac{\nu^3}{\epsilon} \right)^{1/4}, \quad (3.1)$$

where ϵ is the energy dissipation rate, is typically quoted as the smallest length scale that needs to be resolved. ϵ can be expressed as

$$\epsilon = 2\nu \mathbf{S}^2, \quad (3.2)$$

where \mathbf{S} is recognized from equation 2.2 as the traceless rate of strain tensor. $\mathbf{S}^2 = \sum S_{ij}^2$ is a scalar quantity.

This means that the mesh spacing in the grid can not be larger than η in order to resolve the smallest scales. However, as explained by Moin & Mahesh [19], this requirement is probably too strict. It has been shown that as long as the mesh spacing is $O(\eta)$, the resolution is fine enough. As will be shown in section 3.4, this requirement has been fulfilled.

In the same manner, time scales are typically represented by the rotational period of eddies. Then it is obvious that also a wide range of time scales are present in turbulent flows. As shown by Moin & Mahesh [19], the Courant-Friedrichs-Lewy (CFL) number must be sufficiently low to minimize computational error. In the Pencil Code [23], the CFL number is implemented as

$$c_{CFL} = \frac{u_{\max} \Delta t}{\Delta h}, \quad (3.3)$$

where Δt is the time step, Δh is the minimum mesh spacing and $u_{\max} = \max(|\mathbf{u}| + c)$ is the maximum velocity, and c is the sonic speed. The CFL number controls that a fluid element at maximum velocity, including movements in shock waves, cannot go past more than one mesh point within one time step. With $c_{CFL} > 1$ this would be possible, and obviously the code would be numerically unstable. By advice from previous experiences with The Pencil Code, the CFL number used is $c_{CFL} = 0.4$. This means that the time step is given by

$$\Delta t = 0.4 \cdot \frac{\Delta h}{u_{\max}}. \quad (3.4)$$

Because u_{\max} is computed at each time step, Δt is not a constant. For statistically steady flows, however, the variations are small.

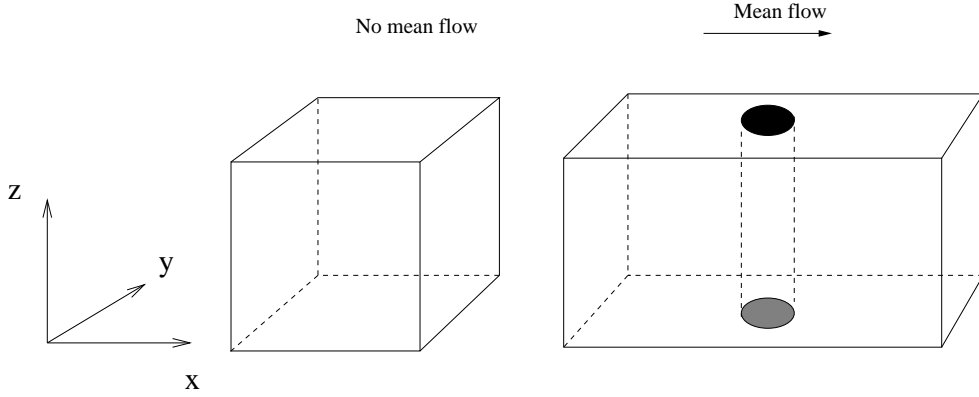


Figure 3.1: Overview of computational domains. In the cubic box (with side lengths L_{xyz}) to the left turbulence is created by forcing at large scale, creating homogeneous, isotropic turbulence. Then this is used as inflow in the main computational domain on the right.

3.4 Initial and boundary conditions

Figure 3.1 gives an overview of the computational domains and the axis directions. First, turbulence is created by forcing in a cubic domain, then this turbulence is used as inflow in the second domain with the cylinder.

When describing side lengths, L_i , repeated indices indicate that the side lengths are equal in size in these dimensions, i.e. L_{ij} indicate that $L_i = L_j$.

3.4.1 Creating turbulence by forcing

In a cubic domain with periodic boundary conditions in all directions and no mean flow, turbulence is created by forced input of energy. The turbulence will, after developing to a statistically steady state, be isotropic and homogeneous. In most applications, for example in a channel or duct flow, the turbulence will have some degree of anisotropy and inhomogeneity. In this study, however, the implementation of the turbulence is desired to be as general as possible.

The forced input of energy is implemented as a body force acting on the fluid, and included in the Navier Stokes equation (2.2). It is the same implementation as used by Pearson et. al. [21], given by

$$\mathbf{f}(\mathbf{x}, t) = \frac{\mathbf{F}(\mathbf{x}, t)}{\rho} = f_0 \mathbf{e} \cos [i\mathbf{k}(t) \cdot \mathbf{x} + i\phi(t)], \quad (3.5)$$

where $\mathbf{k}(t)$ is a wavenumber with direction and magnitude chosen randomly at each time step, but the magnitude is always close to the average (design) wavenumber $k_{n,f}$, i.e. $k_{n,f} - 0.5 < |\mathbf{k}(t)|/k_0 < k_{n,f} + 0.5$. $k_{n,f}$ is given in units of k_n , which is non-dimensionalized by $k_n = k/k_0$. $k_0 = 2\pi/L_{xyz}$ is the wavenumber corresponding to a wavelength equal to the side lengths of the domain, L_{xyz} . $\phi(t)$ is a phase between $-\pi$ and π , and is also chosen randomly at each time step. \mathbf{e} is a random unit vector

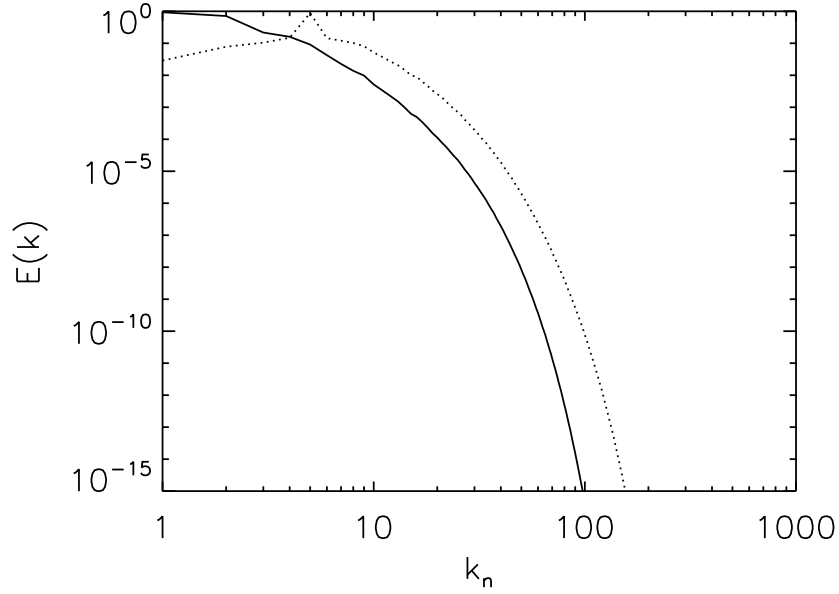


Figure 3.2: Energy spectrum (Fourier decomposition of energy) in a log-log plot. k is normalized by $k_0 = \frac{2\pi}{L_{xyz}}$, where L_{xyz} is the length of the computational domain in all three directions. Energy is forced in to the fluid at $k_n \simeq 1.5$ (solid line) and at $k_n \simeq 5$ (dotted line).

perpendicular to \mathbf{k} , with direction determined by $\phi(t)$. f_0 is the forcing amplitude. Because of the random choices at each time step, the forcing is δ correlated in time. With this implementation of forcing, two parameters determine the behaviour of the turbulence; f_0 and $k_{n,f}$.

Two different scales of forcing are investigated, namely $k_{n,f} = 1.5$ and $k_{n,f} = 5$. The forcing amplitude, f_0 , is chosen to achieve a maximum velocity, u_{\max} , of around 60–80% of the mean flow velocity, \mathbf{U}_0 , in the cylinder simulation.

In figure 3.2 the energy spectra at the two different $k_{n,f}$'s are plotted. We can see that the energy spectra have their maxima at the wavenumbers of the forcing, i.e. at $k_n \simeq 1.5$ and $k_n \simeq 5$. The cascade of energy from small k to large k is as expected for realistic turbulence. From Pope (Turbulent Flows, ch. 6 [1]) we know that isotropic energy spectra should exhibit the power-law behaviour $E(k) \propto k^{-5/3}$, in the inertial range. The inertial range is characterized by length scales l given by $\eta \ll l \ll l_0$, where l_0 is the length of the largest length scales present. This behaviour, also called Kolmogorov scaling, is well established through many experimental and DNS results (see Saddoughi & Veeravalli 1994, figure 9 [9] for a good comparison). However, the exact scaling exponent, $-5/3$, has been subject to discussion however. Kaneda et. al. [26], for example, found the scaling to be $E(k) \propto k^{-5/3-0.1}$. Also, as described by Dobler et. al. [24], a bottleneck effect exists near the dissipation wavenumber. The bottleneck effect can be seen as a positive variation from the power-law behaviour in the lower end of the inertial range.

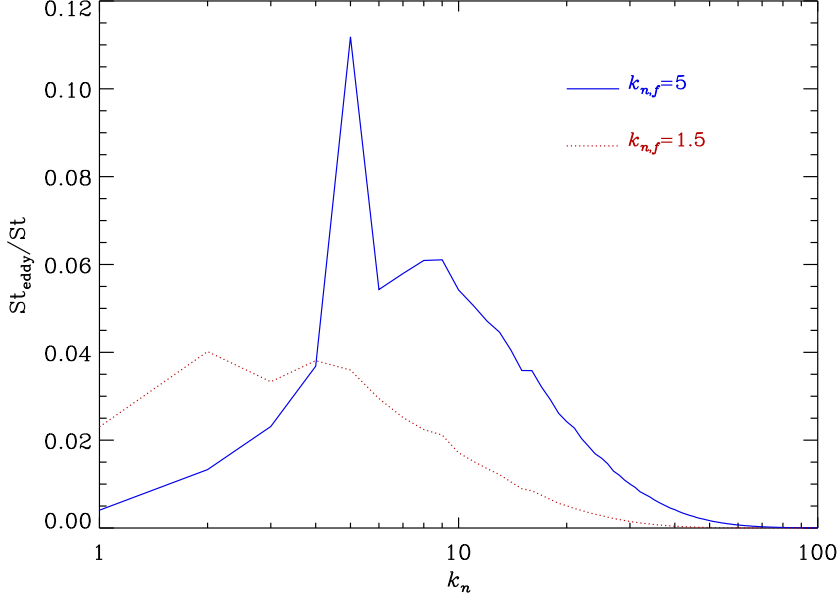


Figure 3.3: Relative Stokes number, St_E/St , as a function of wavenumber.

However, in this case, the scale separation is not big enough to have a sufficiently large inertial range. Thus, the power-law behaviour and bottleneck effect are not observed.

As mentioned in the previous section, in order to resolve all turbulent scales, the mesh spacing, Δh , cannot be larger than $O(\eta)$. In this project, sufficiently resolving the boundary layer around the cylinder sets the strictest requirement on the mesh spacing. And, since the grid resolution of the cylinder flow and turbulent forcing simulations are matched, the mesh spacing of the turbulent forcing is actually smaller than necessary. In the $k_{n,f} = 1.5$ simulation, for example, the ratio of the grid spacing and the Kolmogorov length scale was $\Delta h/\eta = 0.26$. Together with the expected decay of the power spectra seen in figure 3.2, this shows that all turbulent scales are well resolved.

Similar to the regular Stokes number defined for cylinder flow, we can define an eddy Stokes number which express the ratio of the particle response time to the characteristic eddy turnover time, i.e.

$$St_{\text{eddy}} = \frac{\tau_p}{\tau_{\text{eddy}}}, \quad (3.6)$$

which tells us how large or heavy a particle is compared to a turbulent eddy. The characteristic eddy turnover time is defined as

$$\tau_{\text{eddy}} = \frac{l_{\text{eddy}}}{u_{\text{eddy}}},$$

where $l_{\text{eddy}} = L_{xyz}/k_n$ and $u_{\text{eddy}} = \sqrt{2E(k)}$ both varies with eddy wavenumber. It is expected that particles with $St_{\text{eddy}} \gg 1$ will not be affected by the turbulent eddies at

all, while particles with $St_{\text{eddy}} \ll 1$ will follow the eddy streamlines perfectly. From a rather handwaiving argument, particles with St_{eddy} around the order of 1, however, are believed to be subject to different eddy interactions, e.g. centrifuging out of the eddy, that can be relevant to particle deposition. In figure 3.3 the relative Stokes number, St_{eddy}/St , is plotted against wavenumber for the two cases of turbulent forcing. Clearly, St_{eddy} will be smaller than 1 for all particles with $St < 10$. The exception is particles with $St = 10$, that will have $St_{\text{eddy}} \simeq 1$ for $k_n = 5$ eddies from the $k_{n,f} = 5$ turbulence. Particles with $St = 10$ will, however, easily deposit on the cylinder, and the turbulence is not believed to have a large effect on the capture efficiency for them. In general, we conclude that the turbulence studied in this project is not powerful enough to observe eddy stokes numbers larger than or equal to 1. Since the eddy stokes numbers are always small, we expect particle trajectories to be heavily influenced by the turbulence.

3.4.2 Flow around cylinder

The cylinder flow is simulated in a separate domain, with y and z side lengths equal to the forcing domain, but with twice the x side length, i.e. $2L_{yz} = L_x$, see figure 3.1. In this domain a mean flow, $\mathbf{U} = U_0\hat{x}$, is imposed. In y and z directions, boundary conditions are periodic. In the x direction, however, this would not be practical, since we do not want the vortex street of the cylinder to appear at the inlet. The boundary conditions implemented for the x direction are the *Navier-Stokes characteristic boundary conditions* (NSCBC), as described by Poinso & Lele [12] and by Lodato et. al. [8]. NSCBC lets us remove the fluid at the outlet, and we can specify a velocity field at the inlet. With the current implementation in The Pencil Code, we need to make sure that we have no negative velocities at the NSCBC boundaries, which limits the maximum intensity of the turbulence we can insert.

The solid geometry of the cylinder is implemented using the immersed boundary method. Using this method, we account for the solid by adding a virtual force term to the Navier-Stokes equation, equation 2.2. To ensure a sharp wall separating the fluid and the solid, ghost points (grid points) within the cylinder are assigned properties corresponding to their respective mirror points in the fluid. The mirror point is the symmetrically mirrored point, with respect to the boundary surface. This implementation ensures that “passive” gridpoints inside the solid geometry is actively used by increasing the resolution close to the boundary surface. For further information on the solid geometry implementation, see Haugen & Kragset [15].

The pre-produced turbulence from the cubic domain is used as inflow condition in the main domain, looping over the grid planes normal to the flow. The turbulent velocity field is imposed on top of the mean flow, i.e. $\mathbf{u}_{\text{inlet}} = U_0\hat{x} + \mathbf{u}_{\text{turbslice}}$, where $\mathbf{u}_{\text{turbslice}}$ is the velocity field of a yz slice of the cubic domain and $\mathbf{u}_{\text{inlet}}$ is the velocity field of the inflow boundary in the main domain. At the first timestep, the turbulent slice with the largest x value is chosen, $x_1 = x_{\text{max}}$. At the subsequent timesteps, the turbulent slices are chosen according to the distance traveled by the fluid at mean flow for each timestep, i.e. $U_0\Delta t$. The position of the slice to be extracted at timestep i , x_i , is chosen according to $x_i = x_{i-1} - U_0\Delta t$. When the slice position, x_i , does not correspond exactly with a

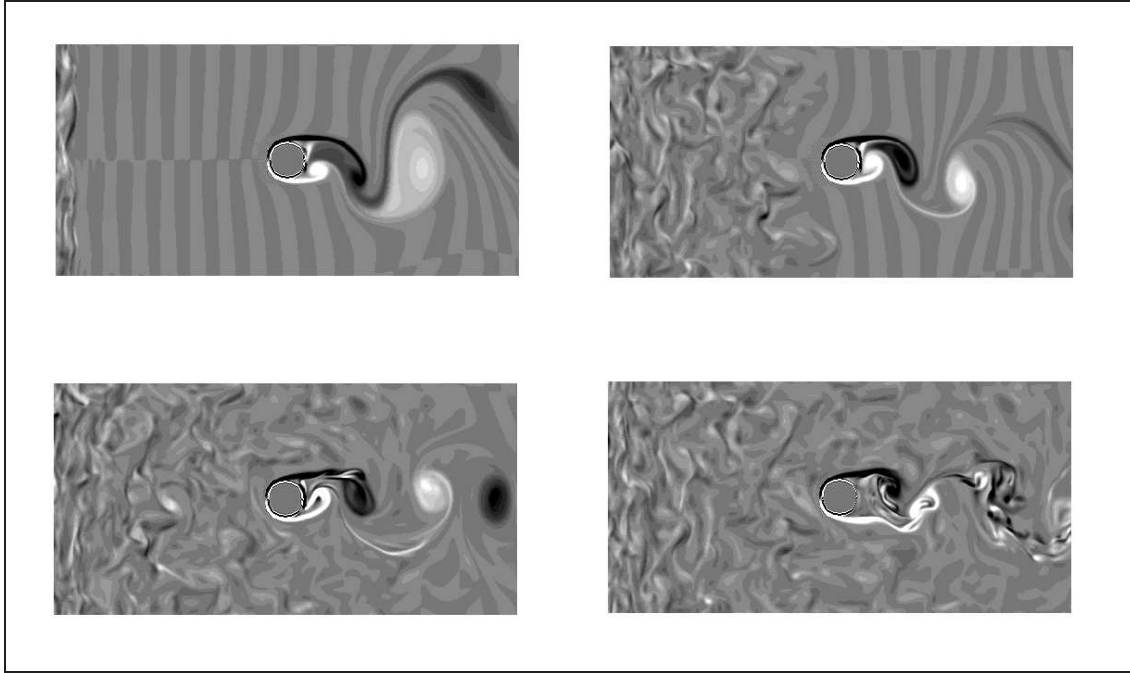


Figure 3.4: Snapshots of the z -component of vorticity, ω_z , in the xy -plane of the main computational domain. This shows how the turbulent inflow interacts with cylinder flow. The turbulent inflow is from a presimulation with forcing at $k_n \simeq 5$.

grid plane (most of the time), $u_{\text{turbslice}}$ is chosen by a linear interpolation between the preceding and succeeding grid planes. When the entire x range of the cubic domain has been covered, the x position jumps back to the start (the periodic boundary ensures that there is no discontinuity). An important note is that this turbulence implementation would not work for a channel or duct flow, where there is a mean flow *profile* rather than a universally constant mean flow.

Figure 3.4 shows how a change from laminar to turbulent inflow evolves through the main computational domain. We can see that the turbulence has a decaying trend. This is due to the energy dissipation of the turbulence, and the fact that there is no energy input. It is assumed that using a superposition of a one dimensional mean flow, $\mathbf{U}_0 = U_0 \hat{x}$, and a turbulent flow field, \mathbf{u}' , is a realistic and correct way of implementing turbulence.

3.4.3 The particles

When the turbulent flow around the cylinder has reached a statistically steady state (lower right snapshot of figure 3.4), particles are released. Particle velocities at release, are set equal to the mean flow velocity U_0 . The boundary conditions for the particles are equal to those of the fluid; the y and z boundaries are periodic, while the particles are removed at the outflow boundary.

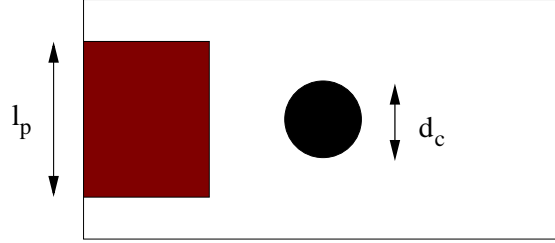


Figure 3.5: Sketch showing the quantities in the capture efficiency formula. l_p is the width of the particle insertion box and d_c is the diameter of the cylinder. When l_p is varying a normalization of the capture efficiency is needed, thus we include $f_A = l_p/d_c$ which says which fraction of particles starts *in front of* the cylinder. (Figure dimensions are not to scale with actual values).

3.5 Capture efficiency

Particles colliding with the cylinder surface are removed and assumed to be deposited. The capture efficiency, η_c , is expressed as

$$\eta_c = \frac{N_C}{N_{\text{init}}} = \frac{N_c}{N} \cdot f_A, \quad (3.7)$$

where N_c is the number of collisions with cylinder and $N_{\text{init}} = N/f_A$ is the number of particles initially in front of the cylinder cross sectional area. N is the total number of particles inserted, $f_A = l_p/d_c$ is the fraction of cylinder diameters, d_c , spanned by the width of particle insertion box, l_p . See figure 3.5 for explanation. l_p is chosen to be sufficiently large, and varies between different turbulent inflows. To make the results comparable, f_A is included to normalize η_c and make the results comparable. A discussion of what is a reasonable value of l_p is included in chapter 4.

3.6 Two dimensional turbulence

Simulating turbulence in three dimensions is very costly in terms of CPU hours. Simulating in only two dimensions would be preferable if the results can be trusted. For this reason, the 3D results produced in this work are compared with results from 2D simulations. As mentioned earlier, turbulence is a three dimensional phenomenon. 2D turbulence can, however, have a physical meaning where one dimension is heavily suppressed by boundaries compared to the other two dimensions. A typical example of this is weather phenomena in planetary atmospheres. The major difference between 2D and 3D turbulence is the energy cascade. In the 2D case larger turbulent scales are generated from smaller scales, which is called an inverse energy cascade [17]. This is in strong contrast to 3D turbulence where the generation of smaller scales eventually leads to energy dissipation.

As shown by Chertkov et. al. [16], a constant forcing in 2D turbulence leads to a growing condensation of energy at the size of the system. For this reason, we cannot pre-produce 2D turbulence by forcing in a 2D simulation, and get comparable results

with the general 3D case. Thus, the turbulent inlet chosen, is just a 2D slice of the turbulent forcing simulation used for the 3D inlet.

Chapter 4

Parameter determination

4.1 Sound speed

As seen from equation 3.4, the sound speed chosen will have an impact on the length of each time step. Choosing a very high speed of sound (e.g. $c = 340$ m/s for a gas similar to air at room temperature) will of course be an intuitive choice, but at a huge computational cost. The Mach number is defined as

$$M = \frac{\max(|\mathbf{u}|)}{c}, \quad (4.1)$$

where \mathbf{u} is the velocity field and c is the speed of sound. It is desired to minimize the magnitude of the sound speed, while the Mach number is still low *enough*. An adjustment in Mach number means, in essence, an adjustment in the compressibility of the fluid, where an increase in Mach number corresponds to an increase in compressibility. We want to maximize the Mach number in order to save computational expenses, but still have results general for weakly compressible flows.

In order to investigate the impacts of the Mach number on the turbulence, and in particular how the inlet boundary condition was able to handle Mach number differences, power spectra from simulations with different sound speeds were compared. For this purpose, two cubic domains with grid resolution $128 \times 128 \times 128$ were used. In the first domain, forcing was included to create turbulence, and all boundary conditions were periodic. In the second domain, this turbulence was used at the inlet, in the same way as turbulence is introduced when simulating with particles. One dimensional power spectra is inspected (Fourier transform in one dimension at a time), because the boundary conditions for the x direction in the second domain are not periodic and thus the power spectra for the x direction are affected by this. Fourier transform only works well for infinite dimension lengths, i.e. periodic boundary conditions, thus the x direction power spectra will be dramatically different than the other two dimensions. The one dimensional power spectra found, are defined as the sum of all single grid line spectra in the given direction.

In figure 4.1, the first simulation with forcing was ran with a sound speed of $c = 20$ m/s, and a forcing amplitude giving $u_{\max} \simeq 2.9$ m/s resulting in a Mach number of

$M = 0.145$. This flow field was then used as inflow in simulations with different sound speeds, ranging from $c = 10$ m/s to 160 m/s. In these simulations the turbulent flow field was put on top of a predefined mean flow velocity of $\mathbf{U}_0 = U_0 \hat{x} = 5$ m/s. Some damping in the NSCBC parameters of the inlet resulted in a maximum velocity of around $u_{\max} \simeq 7.5$ m/s in the second domain. Inspecting the y and z directions in the figure, we can see a converging trend of the power spectra with decreasing Mach numbers. The entire range of turbulent scales is better represented with a smaller Mach number, and more similar to the first simulation with forcing.

In figure 4.2, two different cases are considered. The first simulation with forcing was ran with two different sound speeds, $c = 20$ m/s and $c = 80$ m/s. Both these simulations are used as input in the second domain with $c = 80$ m/s and compared. The reason for this test was to see if a sudden jump in Mach number from one domain to another would have an effect on the power spectra. As can be seen from the figure, the curves show the same behaviour, which justifies choosing a smaller sound speed in the first domain than in the second domain.

From the results presented here, the choice was made to use $c = 20$ m/s for the first domain with forcing, and $c = 40$ m/s for the second domain. The difference in sound speed may appear non-physical, but is justified by figure 4.2, and from figure 4.1 it is concluded that 40 m/s is good enough for representing all scales in the second domain.

There is a discrepancy in the y power spectrum of the forcing domain seen in the figures. Power spectra from x and z directions are more or less equal, indicating isotropy, but the y direction spectrum deviates from the other two (showing a steeper decay in the power spectrum towards the highest wavenumbers). Repeated attempts to find the cause of this discrepancy in the plotting code have not succeeded. Hopefully, the turbulence *is* in fact isotropic, and a bug or error in the plotting code is the cause of this. The fact that the second simulation with turbulent inflow does not converge towards the same deviating spectrum as the forcing in the y direction is a positive indication that this is a post processing error.

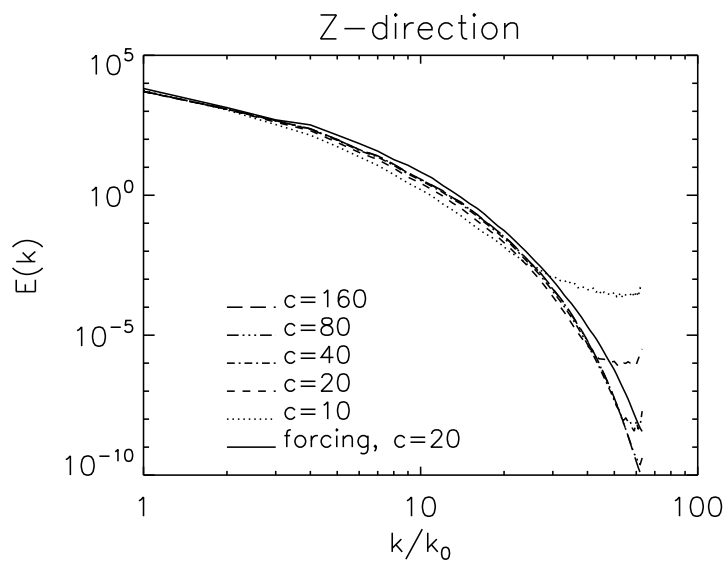
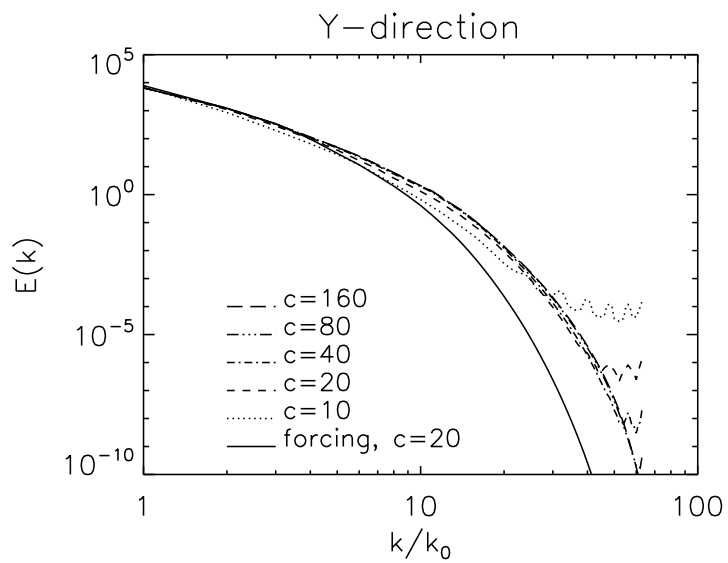
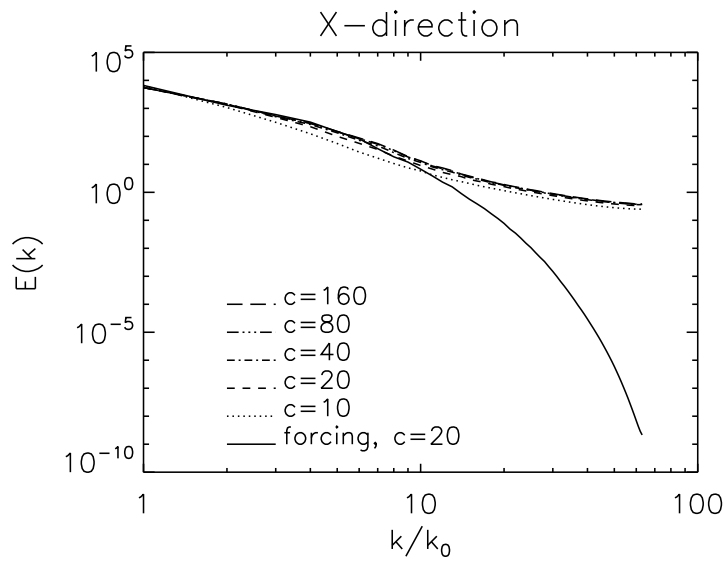


Figure 4.1: One dimensional power spectra for a cubic domain with turbulent inflow. Different sound speeds are compared. The sound speed of the turbulent forcing (at $k_n = 1.5$) is $c = 20$ m/s

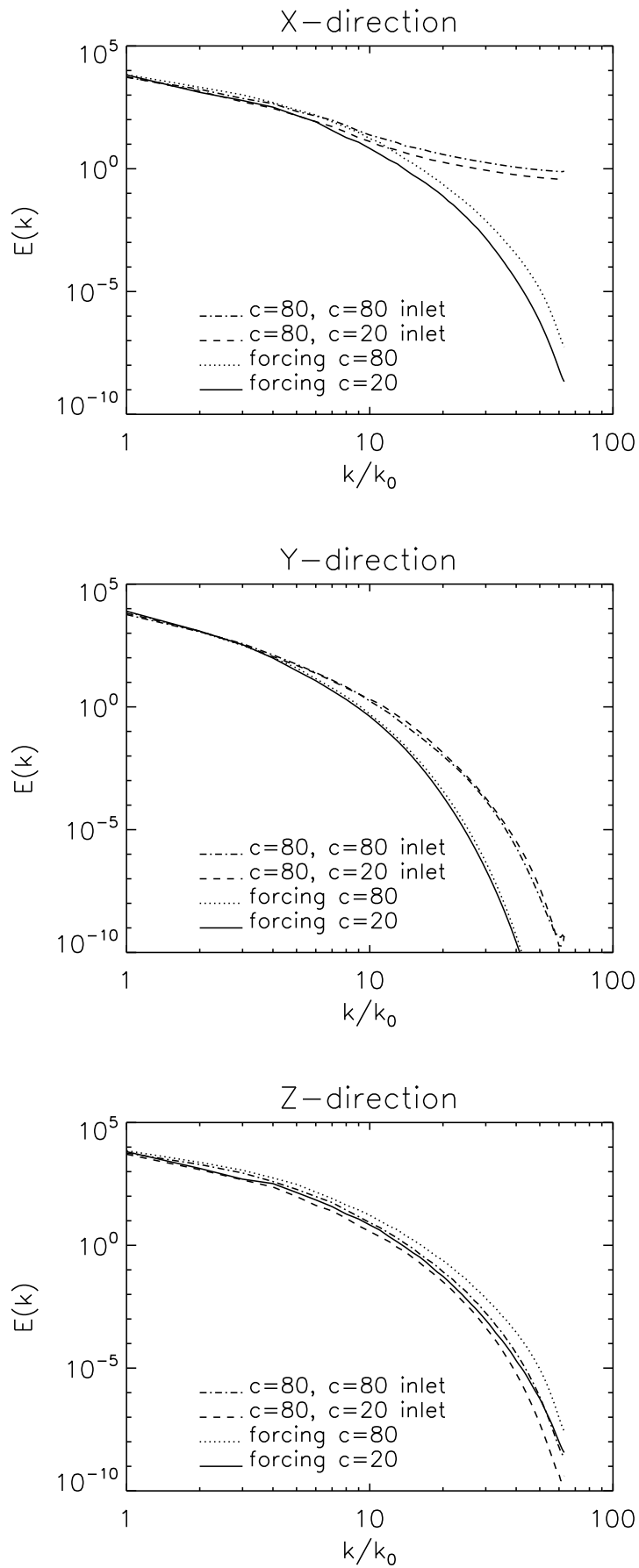


Figure 4.2: One dimensional power spectra for two different forcing simulations, one with $c = 80$ m/s and one with $c = 20$ m/s. And for two simulations with $c = 80$ m/s that use the different turbulence cases as inflow. The purpose of the figure is to validate that two different sound speeds in the two different domains give realistic results.

Table 4.1: Magnitudes of length parameters in units of L_{yz} .

Quantity	Symbol	Magnitude
Cylinder diameter	d_c	0.1685
Particle insertion width, laminar	$l_{p,l}$	0.1685
Characteristic eddy size, $k_n = 5$ turbulence	l_5	0.2
Particle insertion width, $k_n = 5$ turbulence	$l_{p,5}$	0.5
Characteristic eddy size, $k_n = 1.5$ turbulence	$l_{1.5}$	0.667
Particle insertion width, $k_n = 1.5$ turbulence	$l_{p,1.5}$	1.0
Particle insertion length, all cases	$t_{insert}U_0$	0.75

4.2 Particle insertion

Particles should be inserted sufficiently far upstream from the cylinder to make the deposition results independent of initial position and injection velocity. Particles are inserted with a constant number density within a given region, and they need some time to disperse into different regions of the vortical structures, giving a more physical particle position distribution. From this argument, it is concluded that particles will be inserted at the inflow boundary.

The region for the particle insertion must be sufficiently wide, but not larger than necessary, since particles far away from the cylinder will not give any better deposition statistics, and will only consume computational resources. For laminar inflow, the insertion width does not have to be larger than the cylinder diameter, since no particle trajectories will cross the laminar streamlines. For the two cases of turbulent inflow, however, the insertion width must be increased to account for the possibility of eddies transporting particles normal to the mean flow (y direction) into a collisional course.

For forcing at $k_n = 1.5$ the forcing wavenumber corresponds to an integral scale of $l_{1.5} = L/L_{xyz} = 1/1.5 = 0.667$, where L_{xyz} is the side lengths of the cubic domain. L_{xyz} equals L_{yz} in the cylinder computational domain. $k_n = 5$ corresponds to an integral scale of $l_5 = L/L_{xyz} = 0.2$. The insertion widths of the two cases of turbulence are shown in figure 4.3. The width of the particle insertion regions are denoted by $l_{p,l}$, $l_{p,5}$ and $l_{p,1.5}$, which corresponds to laminar, $k_n = 5$ turbulence and $k_n = 1.5$ turbulence, respectively.

Instead of inserting all particles at the first time step, they will be inserted at a constant rate for a certain insertion time, t_{insert} . The magnitude of t_{insert} should be large enough to span over several characteristic turbulent eddy times to give satisfying statistics. Also, t_{insert} should span over several von Karman eddy cycles. In order to limit the running time of the simulations, one t_{insert} was set for all cases; $t_{insert} = 0.75L_{yz}/U_0$.

The magnitude of all particle insertion parameters are given in table 4.1.

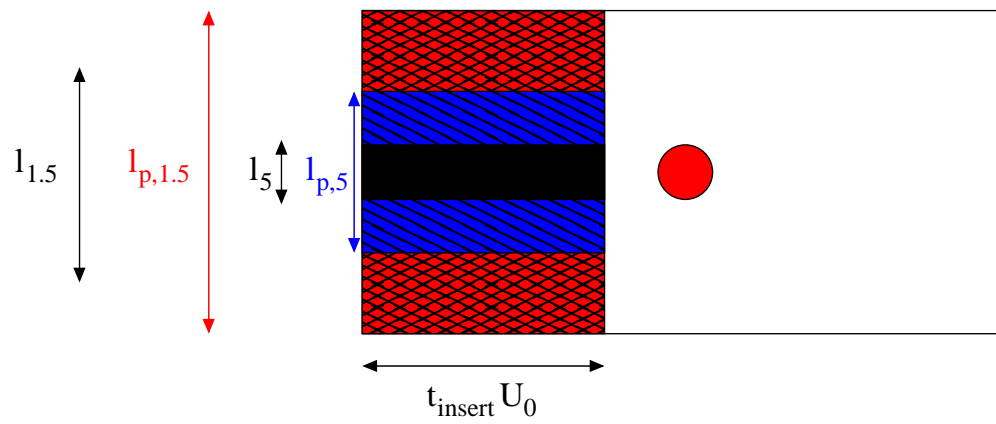


Figure 4.3: Black region shows particle insertion for laminar inflow (equal to cylinder diameter), blue region for turbulent inflow with forcing at $k_n = 5$ and red region for turbulent inflow with forcing $k_n = 1.5$. l_5 and $l_{1.5}$ shows the integral scale for the two forcing scales. The width of the particle insertion regions are denoted by $l_{p,l}$, $l_{p,5}$ and $l_{p,1.5}$, which corresponds to laminar, $k_n = 5$ turbulence and $k_n = 1.5$ turbulence, respectively. The insertion time, t_{insert} , is equal for all cases.

Chapter 5

Results and discussion

5.1 Definition of cases

The present results for turbulent inflow are compared to results from laminar inflow. The Reynolds number for all simulations is $Re_c = 420$. The capture efficiency of particles on the cylinder is recorded and compared between cases. For simulations with turbulent inflow, a cartesian grid of $1024 \times 512 \times 512$ was used. For laminar inflow a 2D grid of 1024×512 was used, unless otherwise specified. Section 5.2 will evaluate the choice of simulating laminar inflow in only two dimensions, by comparing laminar capture efficiencies in 2D and 3D. Section 5.3 will evaluate the independency of grid resolution, by comparing the results from the 2D laminar simulation with results from a high resolution (2048×1024) simulation.

The two cases of turbulence forcing, $k_{n,f} = 1.5$ and $k_{n,f} = 5$, are simulated in cubic domains with a cartesian grid of $512 \times 512 \times 512$. Results from turbulent inflows are presented in section 5.4. The Mach number of the simulations is typically $0.125 < u_{\max}/c < 0.25$. Comparison with relevant experimental results is included in section 5.5. In section 5.6, 2D simulations with turbulent inflow are compared to corresponding 3D simulations. Finally, the results will be discussed in section 5.7. Statistical analysis of the results is not included, due to the main object of the project being of a qualitative nature.

Typically, 64 or 128 CPUs have been used in parallel for 3D simulations. Approximately 180000 CPU hours have been used in total.

5.2 Validation of laminar simulations in 2D

The particle deposition results for turbulent inflow are compared to results for laminar inflow. The laminar inflow simulations are done in 2D. To validate that the laminar simulations are independent of the third dimension, one 3D simulation with laminar inflow was conducted. Figure 5.1 shows the capture efficiencies for the two cases. We can see a good agreement of the results. The different behaviour of the 3D case at the lowest Stokes numbers ($St = 0.1$ and $St = 0.05$) are probably caused by poorer statistics.

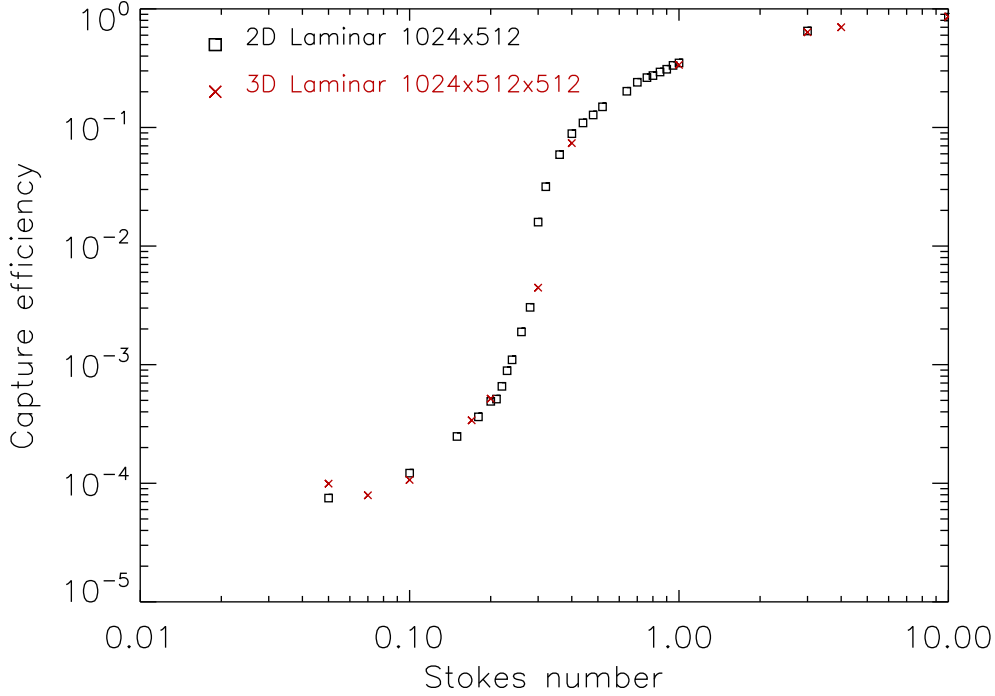


Figure 5.1: Capture efficiencies, η_{front} , for laminar inflow, 2D and 3D simulations compared. Generally, a good agreement is observed. The statistics for the 3D simulation at the lowest Stokes numbers is not very good.

Table 5.1: Back side capture efficiency for $St = 0.1$

Simulation case	Particles inserted	Particles deposited on back side	η_{back}
2D 1024×512	$2.88 \cdot 10^5$	8	$\simeq 3 \cdot 10^{-5}$
3D $1024 \times 512 \times 512$	$2.25 \cdot 10^5$	0	0

Less than 50 particles are deposited at these Stokes numbers, thus the uncertainty is higher. The overall agreement between the curves is good, and this justifies the current choice of simulating laminar inflow in only two dimensions.

For capture efficiency on the back side of the cylinder, η_{back} , we do not see the same agreement between 2D and 3D simulations. Because of the low magnitudes of η_{back} observed, the statistics are not good enough to make general conclusions. However, the 2D simulation shows a peak of back side capture efficiency for $St = 0.1$. Results from Haugen & Kragset [15] correspond well with this. For the 3D simulation, no particles deposit whatsoever on the back side. Results for $St = 0.1$ are presented in Table 5.1. As explained in section 1.3, the cylinder wake will have three dimensional effects at $Re_c = 420$. The present comparison might indicate that 2D simulations will over predict back side capture efficiency.

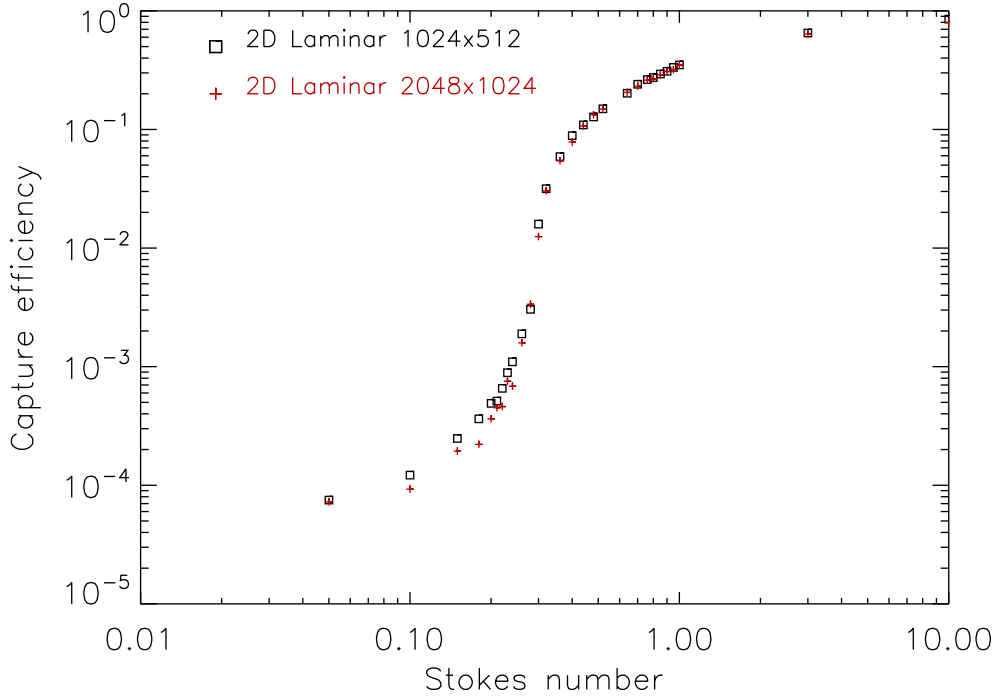


Figure 5.2: Capture efficiency, η_{front} , comparison between different grid resolutions. Results from a simulation with grid resolution 1024×512 (\square), which is used for producing results for laminar inflow, is compared with results from a simulation with grid resolution 2048×1024 (+).

5.3 Validation of grid resolution

The 3D simulations with turbulent inflow have a grid resolution of $1024 \times 512 \times 512$, and the 2D simulations with laminar inflow have a grid resolution of 1024×512 . To make sure the boundary layers around the cylinder are well resolved, a high resolution 2D simulation (2048×1024) have been conducted. Results for capture efficiencies are presented in figure 5.2. The smallest particles would be expected to be more sensitive to changes in roughness of the cylinder boundary, due to their tendency to follow the fluid streamlines. Small changes in the fluid behaviour at the immediate vicinity of the cylinder could potentially mean a large difference in particle deposition for the smallest particles. We can see from the figure that some minor differences are seen for the smallest Stokes numbers up to $St = 0.25$, but no drastic differences are observed. The overall agreement between the results is very good, indicating that the capture efficiency is independent of grid resolution. For the present Reynolds number, $Re_c = 420$, we can conclude that the resolution of 1024×512 is high enough to produce grid independent results for particle capture efficiencies on the cylinder.

5.4 Results with turbulent inflow

Results from the turbulent inflows are presented in figure 5.3a. Capture efficiencies from the two turbulent simulations approach η_{laminar} for the largest Stokes numbers, and for the lowest Stokes numbers. But for the range in between a significant difference is seen. To get a better understanding of the differences, figure 5.3b plots the relative differences between the turbulent cases and the laminar case. The relative difference for turbulent case i , is given by

$$d_i = \frac{\eta_i - \eta_{\text{laminar}}}{\eta_{\text{laminar}}}. \quad (5.1)$$

In figure 5.3b we can see a peak of almost 1000% difference for $k_n = 1.5$ turbulence. The $k_n = 5$ turbulence has a peak value of around 700% difference compared to η_{laminar} . The difference peak is narrower for $k_n = 5$, however, as we can see that the $k_n = 1.5$ difference peak extends more towards smaller Stokes numbers.

To get a better understanding of the differences observed in capture efficiency, the distribution of angles has been recorded. Each particle deposition position is stored, by recording the cylinder angle, θ , at which the deposition occurred. The cylinder angle is defined by figure 5.4, where $\theta = 0$ corresponds to the cylinder centerline anti-parallel to the mean flow. Since the deposition is assumed to be symmetric with respect to the cylinder centerline, only the absolute value of θ is stored. For each value of θ we can define the deposition number, $\hat{n}(\theta)$, as the number of particles deposited at that angle. To get intuitive plots of the deposition angle distribution, a discretization of $\hat{n}(\theta)$ is needed, i.e.

$$n(\theta_i) = \int_{\theta_i - \Delta\theta}^{\theta_i + \Delta\theta} \hat{n}(\theta) d\theta, \quad (5.2)$$

where $2\Delta\theta$ is the discretization interval. $\Delta\theta = 1^\circ$ was found to be a reasonable discretization. In addition, a normalization of $n(\theta_i)$ is needed to account for the different particle insertion dimensions for the different simulations (as described in section 4.2). For the laminar and turbulent $k_n = 5$ case, $n(\theta_i)$ have been normalized to match the $k_n = 1.5$ case.

Figure 5.5 shows plots of deposition angle distribution for four different Stokes numbers. Note that in addition to the discretization mentioned, the $n(\theta_i)$ elements are smoothed (averaged) over neighbouring elements, giving a total smoothing interval of 6° . The smoothing is included to give more intuitive plots for qualitative considerations, at perhaps the cost of mathematical correctness. At $St = 0.48$, lower right plot, the capture efficiency is roughly the same for the three cases. It can be seen that the depositions have relatively equal angle distribution as well, but the turbulent results have a slightly wider angle distribution. $St = 0.28$, lower left plot, is the Stokes number where the relative difference between $k_n = 5$ turbulence and laminar capture, d_{k5} , has its peak. The $k_n = 1.5$ turbulence have roughly the same value in capture efficiency at this Stokes number, but as we can see from the figure, the angle distribution has a lower maximum at the lower angles, but stretches out to wider angles, compared to the $k_n = 5$ case.

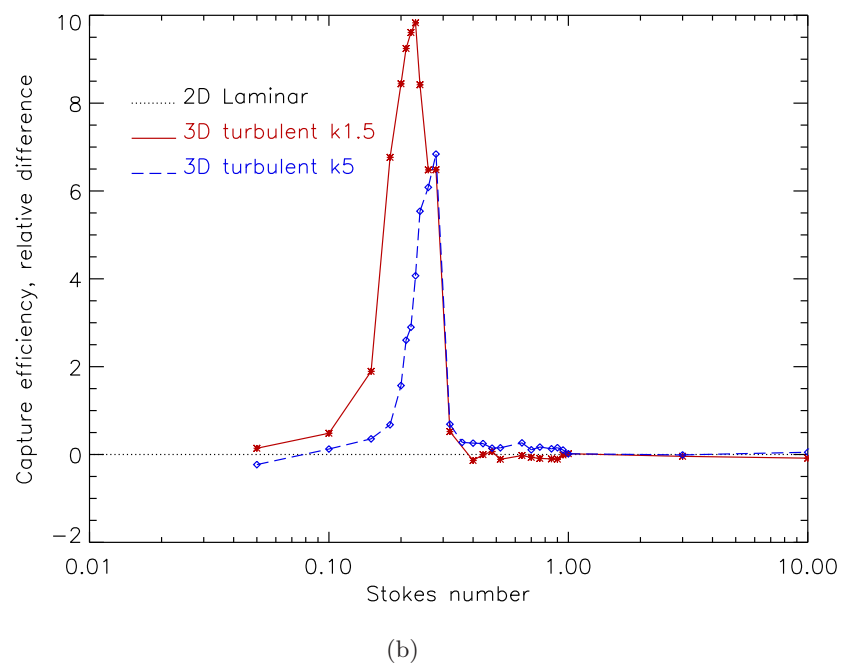
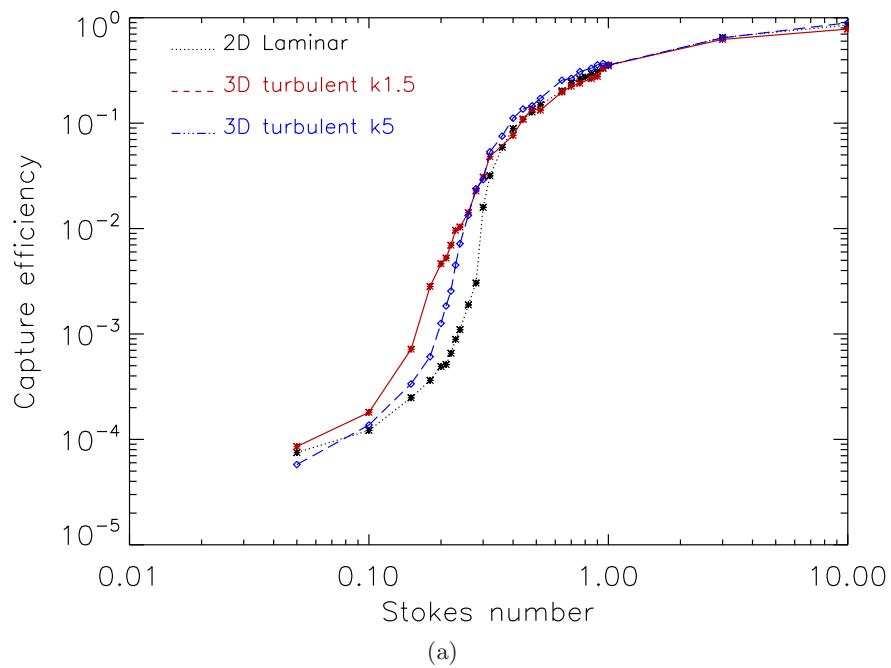


Figure 5.3: Figure (a) shows front capture efficiencies for $Re_c = 420$ and forcing at $k_n = 5$ (blue curve), $k_n = 1.5$ (red curve), laminar inflow (dotted black). Figure (b) shows the relative differences, d_i , between the turbulent and laminar inflows.

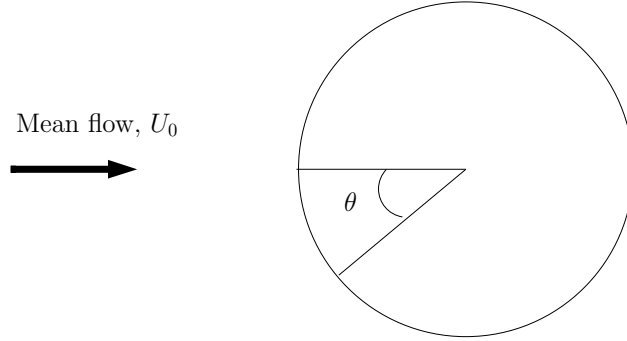


Figure 5.4: Cylinder angle, θ , where $\theta = 0$ defines the centerline of the cylinder, anti-parallel to the mean flow. Only the absolute value of θ is recorded.

In the top right plot, we can see the angle distributions for $St = 0.23$, which is the peak of the relative difference for $k_n = 1.5$ turbulence. At this Stokes number, the laminar deposition is limited to angles lower than $\theta = 20^\circ$. Depositions for $k_n = 5$ goes slightly wider, to $\theta = 25^\circ$, and much more frequent within the same area. The red curve for $k_n = 1.5$ depositions the widest, to about $\theta = 35^\circ$, and significantly higher than the two other cases. All cases seem to have a maximum deposition at around $7 - 9^\circ$. At $St = 0.18$, top left plot, the relative differences are $d_{k1.5} \simeq 7$ and $d_{k5} \simeq 1$. As opposed to the higher Stokes numbers, the angle distributions at this Stokes number have the same widths, up to around $\theta = 25^\circ$. $n(\theta)$ shows the same shape for all cases as well, but the different amplitudes gives the different capture efficiencies.

The local minimum point seen in figure 5.5 at around $\theta = 12^\circ$ for the laminar results, as well as for the turbulent cases for the lowest Stokes numbers, is probably related to the resolution of the simulation. Deposition angle distribution for a laminar inflow is assumed to have a continuous and well behaved curve, thus the local minimum point appears to be non-physical. The fact that the immersed boundary method used to represent the cylinder at the cartesian grid is not perfect, but limited by the mesh spacing, can probably explain this.

Haugen & Kragset [15] define three different impaction modes for different regions of the Stokes number, for laminar inflows. The particles with largest Stokes numbers, $St > 0.5$ (for $Re_c = 420$), are captured because of the *classical impaction* mode, according to Haugen & Kragset. In this mode, the particles have enough inertia to penetrate the boundary layer. For Stokes numbers in the range $0.2 < St < 0.5$ they define a *boundary stopping* mode, where particles start lacking sufficient inertia to penetrate the boundary layer. Particles in the smallest Stokes number range, $St < 0.2$, are believed to be deposited due to the *boundary interception* mode where the particles follow the fluid flow almost perfectly, but some are still impacted due to their finite radii touching the cylinder. From figure 5.3a we can see that the capture efficiency is extremely dependent on the Stokes number in the boundary stopping regime, spanning almost three orders of magnitude. We can also see that it is in the lower end of this regime where the turbulent deviations are largest. In the boundary interception and classical impaction

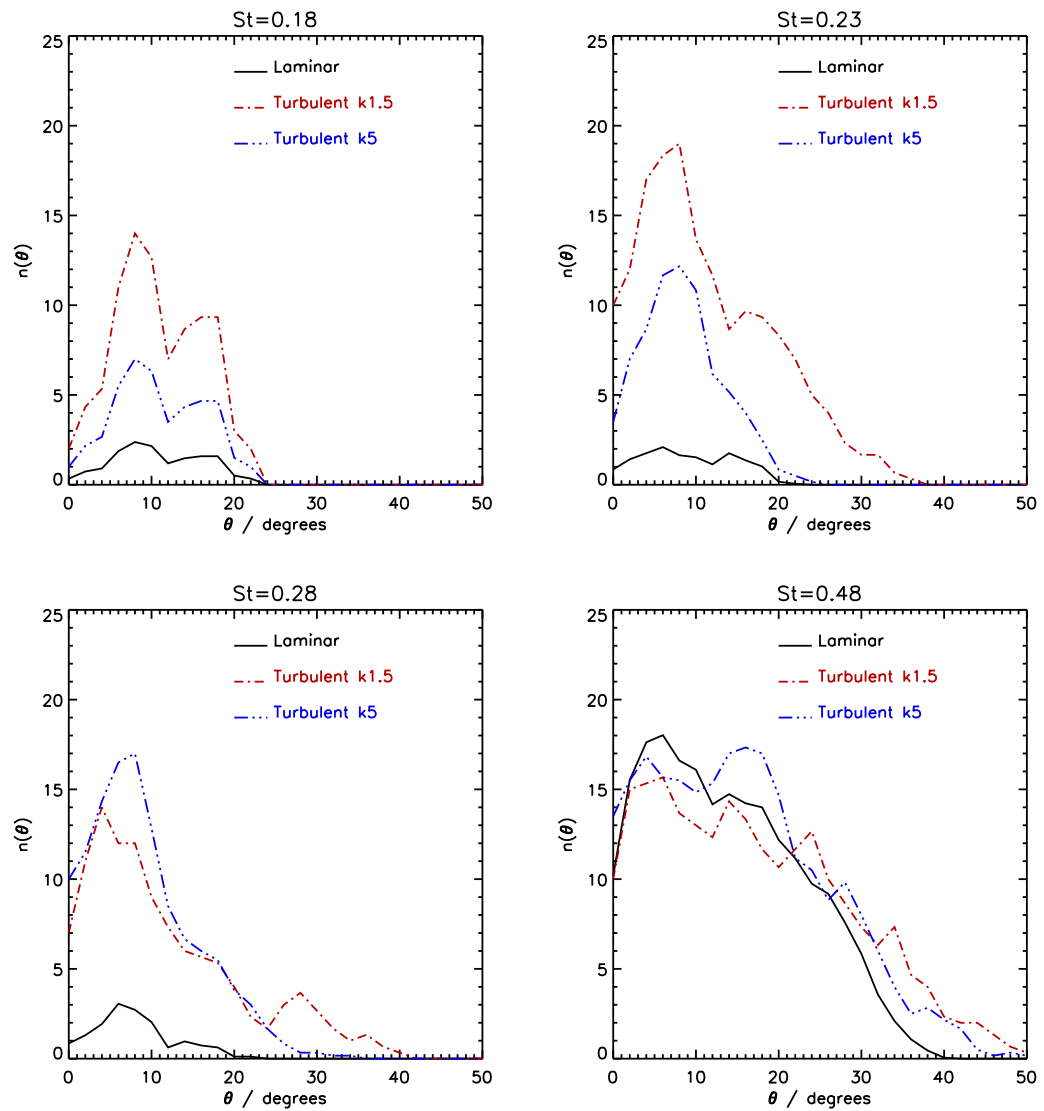


Figure 5.5: Deposition density distributions, $n(\theta)$, for the different cases. Four different particle sizes are plotted.

modes, however, the results from turbulent inflows are similar to the laminar result. The smallest particles inspected here, with $St = 0.05$, are in the upper end of the boundary interception range, thus general conclusions for the entire boundary interception mode cannot be made. However, the trend seen in figure 5.3a agree well with Haugen & Kragset, which have inspected particles down to $St = 0.01$. It is believed that the turbulence does not change the nature of the boundary layer around the cylinder to a large extent, therefore the capture efficiency in boundary interception mode is assumed to stay roughly the same.

Figure 5.6 shows the average time spent in the fluid for particles that are deposited on the cylinder as a function of Stokes number. The time axis is normalized by $\tau_f = r_c/U_0$, where $t/\tau_f = 0$ is the average time of particle insertion. At mean velocity, U_0 , the fluid spends about $t/\tau_f = 10.9$ from inlet to cylinder front. We can see that the smallest particles spend more time in the fluid than the larger ones. This is because the smallest particles slow down in the boundary layer. For the largest Stokes numbers, $St > 0.5$, the particle time logically approaches the mean flow time, since initial particle velocity equals U_0 .

Interestingly, particles in the $k_n = 1.5$ turbulent case have a minimum point of time spent lower than the mean flow time. This means that the deposited particles must have been accelerated streamwise by the turbulent eddies present. This region of net-accelerated particles stretches from about $St \simeq 0.15$ to $St \simeq 0.25$, and this region coincides perfectly with the region where the $k_n = 1.5$ turbulence have larger deposition than the $k_n = 5$ case. At the minimum point in the $k_n = 1.5$ curve, at $St = 0.23$, the average time spent in the fluid is about $t/\tau_f = 9$, which means they had an average velocity of around 20% more than U_0 .

5.5 Comparison with experimental results

Figure 5.7 compares the capture efficiencies found with other relevant results. Ranz & Wong [5] experimentally found the capture efficiency within the Reynold's number range $62 < Re_c < 500$. They worked with aerosol particles of glycerol with diameter between 0.3 and 1.4 μm produced by a smoke generator. The inflow was laminar, and their smaller particle density relative to the fluid density, ρ_p/ρ , may indicate that lift forces played an important role. Their results have been acquired from the article of Davies & Peetz [18]. Muhr [25] presents an empirical fit model to laminar particle deposition for the Reynold's number range $50 < Re_c < 500$. Muhr's theoretical expression was found in Kasper et. al. [7]. Both works focus on large Stokes numbers, and show relatively good agreement with the results from the laminar simulation in this work.

The turbulent data from Douglas & Ilias [14] are also presented in the figure. They injected aluminum silicate pigments in the flow and recorded the deposition on steel cylinders. The variations between laminar and turbulent capture efficiencies observed in this work are only minor compared to the differences seen in Douglas & Ilias. At least two factors can explain this, however. Firstly, the Reynolds number in Douglas & Ilias' experimental rig is much higher. The turbulence is created by a duct flow,

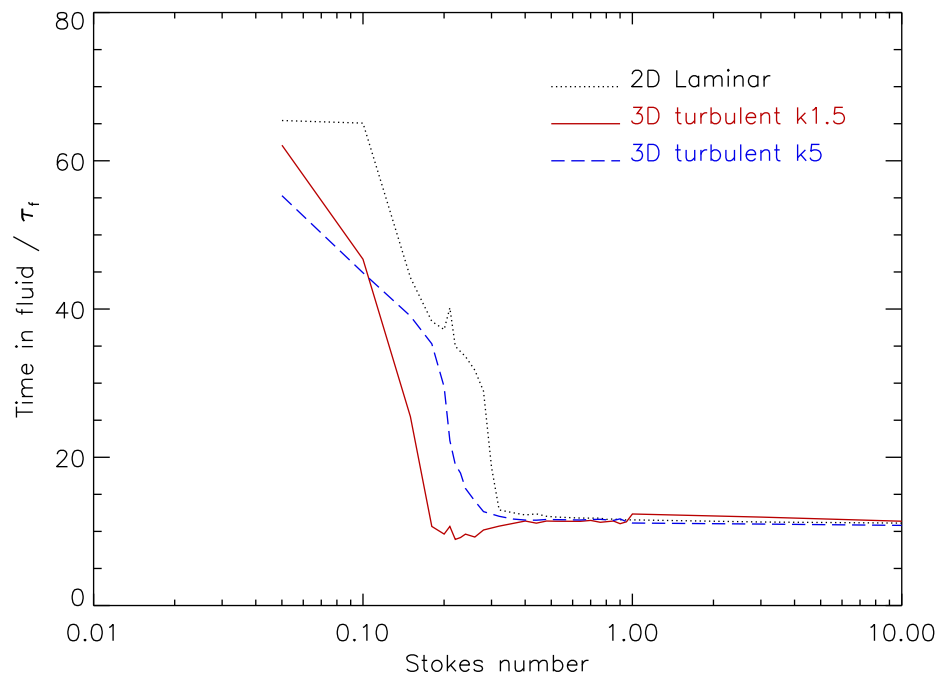


Figure 5.6: Average time spent (in units of $\tau_f = r_c/U_0$) in the fluid before deposition for different Stokes numbers. $t/\tau_f = 0$ is the initial time of the simulation. At mean velocity, U_0 , the fluid spends about $t/\tau_f = 10.9$ from inlet to cylinder front. Note that the minimum point of the $k_n = 1.5$ turbulence around $St = 0.20$ is below $t/\tau_f = 10.9$.

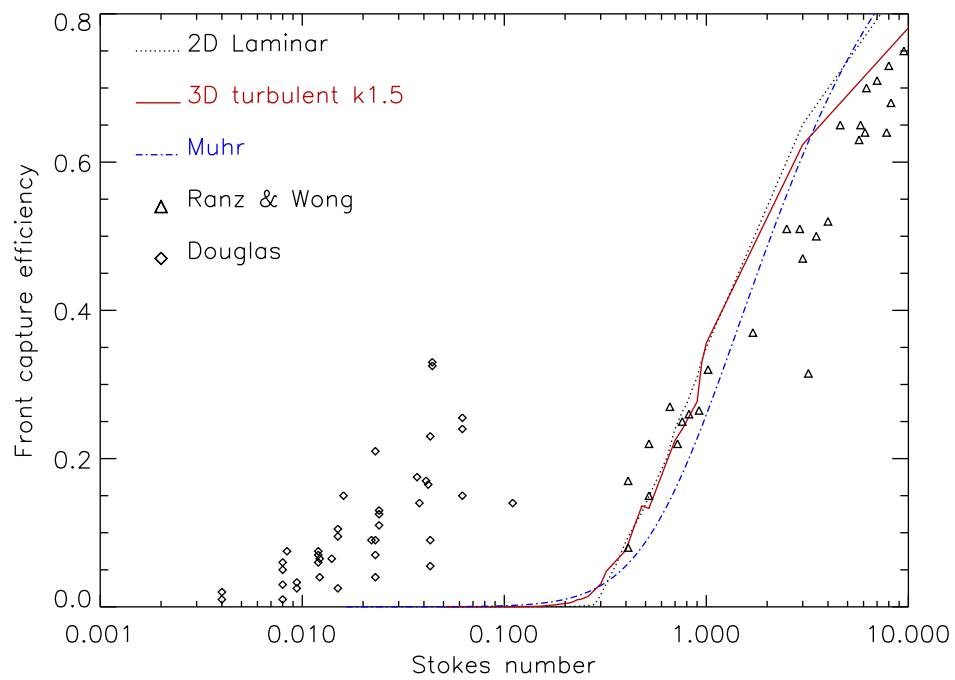


Figure 5.7: Comparison of results with experimental data of Ranz & Wong (1952), Douglas & Ilias (1988) (turbulent) as well as the empirical model of Muhr (1976)

with $Re_D = DU_0/\nu$ ranging from 20000 to 140000. With the cylinder diameter used, this corresponds to cylinder flow Reynolds number, Re_c , ranging from 170 to 7120. The capture efficiency results are plotted without distinguishing the different Reynolds numbers, and are probably a mix within the specified range. The large difference between the Reynolds number in the present work, $Re_c = 420$, and in Douglas & Ilias at up to $Re_c = 7120$, is probably the main reasons for the drastically different results.

Secondly, the present results do not simulate all possible deposition mechanisms. Only drag force is considered, and even if 100% sticking efficiency is assumed, other mechanisms can increase the capture efficiency. Thermophoresis and depositions due to Brownian motions are believed to play a role, and this can be a plausible explanation of the higher deposition seen in Douglas & Ilias.

It is important to note that Muhr defines the Stokes number, equation 2.14, with cylinder diameter instead of cylinder radius. This means that the Stokes number used here has half the magnitude of the Stokes number used in Muhr, for the same particle size. Douglas & Ilias define what they call impaction parameter, Ψ , which also has this factor two difference with the Stokes number definition used here. This difference have been taken into account in figure 5.7.

5.6 Turbulent inflow simulated in two dimensions

As explained in section 3.6, huge computational costs can be saved if 2D simulations are sufficient. We know that turbulence is three dimensional, and the exact same results are not expected. But if simulations in 2D give roughly the same results as in 3D, it will be useful to conduct 2D simulations for investigation of behaviour and trends of turbulent particle deposition. Figure 5.8 presents results from 2D simulations with turbulent inflows. The results show relatively good agreement with turbulent 3D simulations for the largest Stokes numbers down to about $St = 0.25$. At Stokes numbers lower than this, the 2D simulations under predict the capture efficiency compared to the 3D simulations. The sudden jump in capture efficiency from $St = 0.95$ to $St = 1.0$ shows that the uncertainty in turbulent simulations is larger for 2D simulations. This is probably related to the difference in the 2D slice introduced at the inlet (the same 2D slice is used for both simulations, but particles are introduced at different positions in the 2D slice). The 3D simulations use the entire pre-forcing domain ($512 \times 512 \times 512$) as inflow, and all 512 possible “2D-slices” are present. Thus, in addition to more realistically simulating the turbulence in all its three dimensions, the 3D simulations average over 512 different xy -planes, giving more reliable results.

The largest difference seen for turbulent results in 3D is for $k_n = 1.5$ turbulence between $St = 0.15$ and $St = 0.25$. This clear difference is not seen in the 2D results presented here. Maybe this difference could be seen in 2D if the turbulence was introduced in another way. Turbulence snapshots are always seemingly random, and to get reliable results, one must average over many random snapshots. 2D simulations could maybe give better results if the turbulent inflow was continuously changing (not just over a relatively short period), and if particles were inserted over a larger time span. But

further investigation of this is outside the scope of this project. We can conclude that qualitative considerations may be made from 2D simulations, but one must be careful making general conclusions without 3D confirmation.

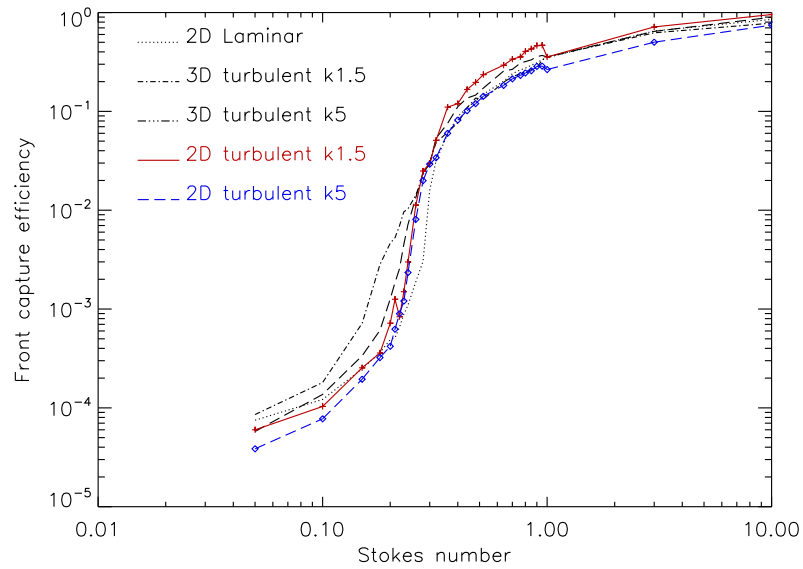
5.7 Discussion

Simulations of particle deposition on a cylinder in laminar flow, produced similar results in 2D and 3D. It is concluded that 2D simulations are sufficient for finding front side capture efficiency. For back side depositions, however, further comparison between 2D and 3D simulations are needed before verifying the use of 2D simulations at the present Reynolds number, $Re_c = 420$. The independency of grid resolution was shown by comparison with results from a simulation with twice the grid resolution. This indicates that the boundary layer around the cylinder is well resolved at the chosen resolution of $1024 \times 512(\times 512)$.

The introduction of turbulence at the inlet increased the particle capture efficiency for particles in the range $0.15 < St < 0.4$. One possible explanation for the different capture efficiencies seen for turbulent inflow is a change in the nature of the boundary layer around the cylinder. If the turbulent eddies deform the boundary layer from time to time, bringing particles closer to the cylinder than usual, an increased capture efficiency would be expected. But if this was the case, we would expect higher capture efficiency also for the smallest particles, in the boundary interception range. The trend seen from the present result, at the upper end of the boundary interception range, does not indicate any differences here. Figure 5.9 shows vorticity contours for laminar inflow, as well as $k_n = 1.5$ turbulence inflow. We can see that the vorticity is much stronger in the boundary layer than outside. Figure 5.10 shows contours zoomed in around the cylinder. The boundary layer on the cylinder front side looks very similar for the two cases. The structure of the back side boundary layer and wake is altered, but this will probably not have any effect on the front side capture efficiency.

If we assume that the boundary layer is not altered to a significant degree, how can we explain the differences seen? Figure 5.6 gives a strong indication that velocity changes play an important role. As a rough estimation, we can maybe divide our flow into two parts; Free fluid flow and boundary layer. If the introduced turbulence only can change the first part, the free fluid flow, then the turbulence can in essence only do two things to affect the particle deposition. It can change the *direction* of particle velocities into the boundary layer, and it can change the *magnitude* of particle velocities into the boundary layer. The latter will probably give a larger effect, since a change in incoming direction only means another path through the boundary layer. Changes in incoming directions can, however, be an explanation of why the angle density distributions, $n(\theta)$, are wider for the turbulent cases.

The Stokes number tells us how heavy a particle is relative to flow geometry, but it does not tell us the exact velocity of a particle. For laminar flows, particles far from boundary layers will approach the mean flow velocity, U_0 , which is included in the Stokes number. When turbulent structures disturb the particle velocity, however, this will not



(a) Capture efficiencies

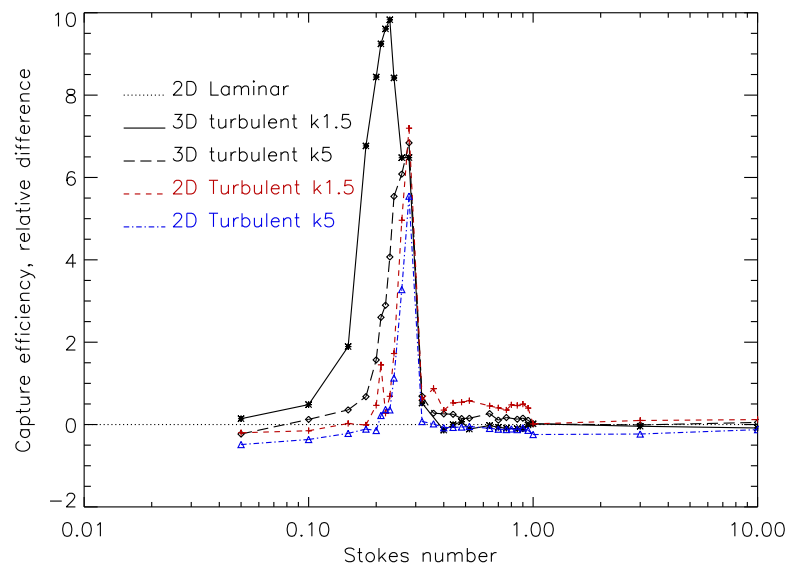
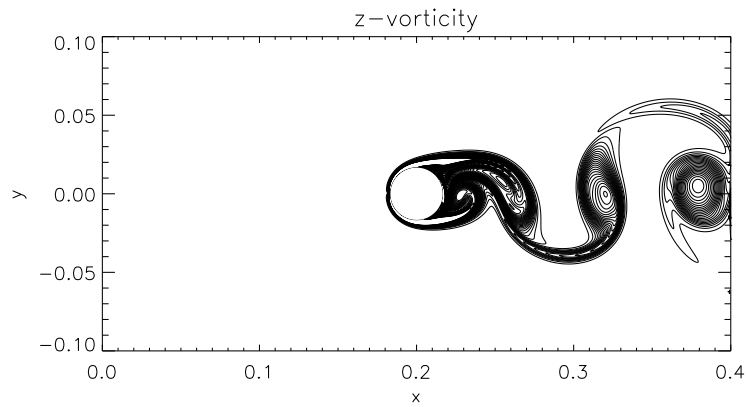
(b) Relative differences, d_i .

Figure 5.8: Capture efficiency (a) and relative differences in capture efficiency (b). Red curve for $k_n = 1.5$ turbulence in 2D, blue curve for $k_n = 5$ in 2D.



(a) Laminar

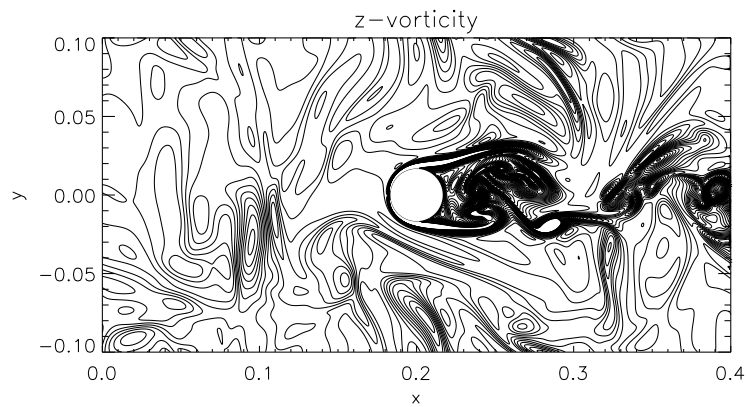
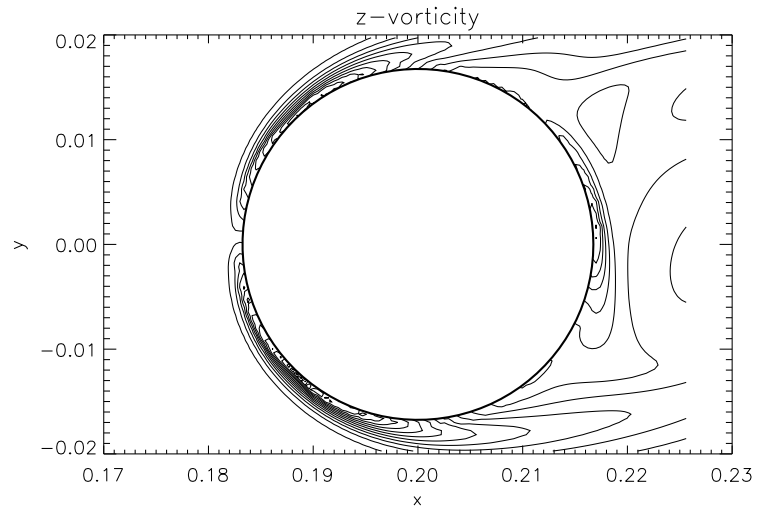
(b) $k_n = 1.5$ turbulence

Figure 5.9: Contours of z vorticity, ω_z , for laminar and $k_n = 1.5$ turbulent inflow. The vorticity in the boundary layer is stronger than in the free flow.



(a) Laminar

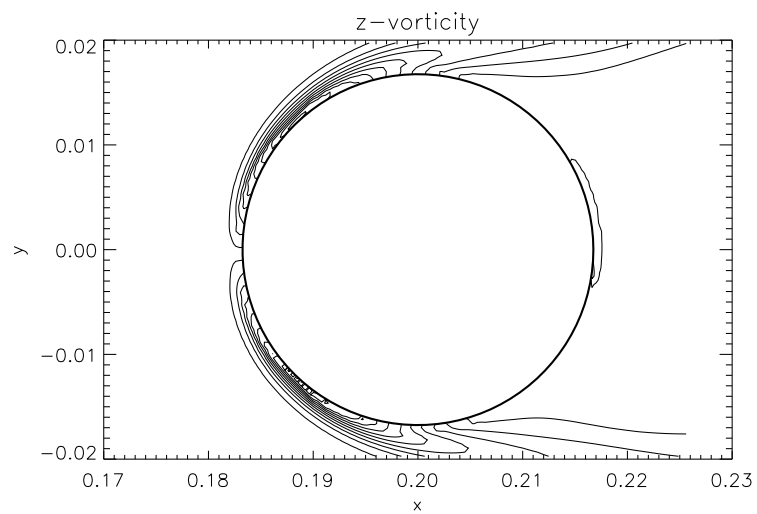
(b) $k_n = 1.5$ turbulence

Figure 5.10: Contours of z vorticity, ω_z , for laminar and $k_n = 1.5$ turbulent inflow, zoomed at cylinder. The front side boundary layer looks very similar for the two cases.

Table 5.2: Capture efficiencies, η_{front} , for laminar and $k_n = 1.5$ turbulent inflows. The value for $\text{St} = 0.29$ (in *italic*) has been found by interpolation.

Inflow	St = 0.23	St = 0.24	St = 0.26	St = 0.28	St = 0.30	St = 0.29
$k_n = 1.5$	$9.6 \cdot 10^{-3}$	$1.04 \cdot 10^{-2}$	$1.41 \cdot 10^{-2}$	$2.28 \cdot 10^{-2}$	$3.08 \cdot 10^{-2}$	-
Laminar	$9 \cdot 10^{-4}$	$1.1 \cdot 10^{-3}$	$1.9 \cdot 10^{-3}$	$3.0 \cdot 10^{-3}$	$1.59 \cdot 10^{-2}$	<i>$9.4 \cdot 10^{-3}$</i>

be included in the regular expression for the Stokes number. If we assume that the inertia of a particle, $P = m_p v$, tells us of how far a particle can penetrate into the boundary layer, then an increased velocity would give equal results to an increased mass. We saw in figure 5.6 that certain deposited particles were about 20% faster than U_0 from inlet to cylinder, on average. This indicates that particles with higher velocity have a higher probability of deposition. Equation 2.14 defined the Stokes number as

$$\text{St} = \frac{\rho_p d_p^2 U_0}{18 \rho \nu r_c}.$$

Particles having different velocities than U_0 when approaching the vicinity of the cylinder, will maybe have an effective Stokes number comparable to

$$\text{St}_{\text{eff}} = \frac{\rho_p d_p^2 V_p}{18 \rho \nu r_c},$$

where V_p is the streamwise particle velocity when entering the boundary layer. The relative difference in capture efficiency for $k_n = 1.5$ turbulence, $d_{k1.5}$, has a maximum at $\text{St} = 0.23$. The turbulent capture efficiency for this Stokes number, is approximately equal to the laminar capture efficiency at $\text{St} = 0.29$, as seen from table 5.2. The suggested effective Stokes number will then be $\text{St}_{\text{eff}} = 0.29$, which gives a particle velocity of $V_p = 1.26U_0$. The simulation with turbulent forcing at $k_n = 1.5$ has root mean square velocity $u_{\text{rms}} = 1.48$ m/s. With $U_0 = 5.0$ m/s, the suggested particle velocity entering the boundary layer will be $V_p = 6.30$ m/s. That is close to $U_0 + u_{\text{rms}} = 6.48$ m/s, which would be an expected average particle velocity.

To investigate the effect of increased velocity, we can define two estimates of effective Stokes numbers, $\text{St}_{\text{eff,A}}$ and $\text{St}_{\text{eff,B}}$, with corresponding particle velocities $V_p = U_0 + u_{\text{rms}}$ and $V_p = U_0 + u_{\text{max}}$, respectively. Effective Stokes number B corresponds to particle velocities increased by the maximum magnitude of the turbulent velocity fluctuations, i.e. $u_{\text{max}} = \max(u')$. Figure 5.11 shows relative differences for these two estimates of the effective Stokes number, where the capture efficiencies have been found by shifting the laminar capture efficiency results according to

$$\eta_{\text{eff}}(\text{St}_{\text{eff}}) = \eta_{\text{lami}} \left(\text{St} \frac{V_p}{U_0} \right).$$

Obviously, these estimates are poor, since particles will be accelerated in all directions, not only streamwise. But what we can interpret from this, in essence, is the capture

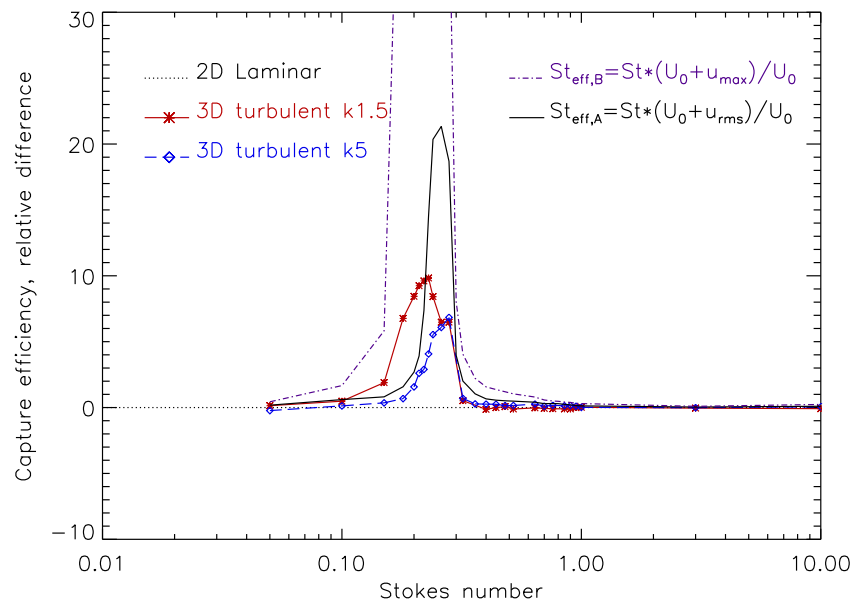


Figure 5.11: Relative differences in capture efficiency, compared to laminar inflow, η_{lami} . The two estimates of an effective Stokes number, $St_{\text{eff,A}}$ and $St_{\text{eff,B}}$, are found by exchanging the mean flow velocity in the Stokes number expression with $U_0 + u_{\text{rms}}$ and $U_0 + u_{\text{max}}$, respectively. The maximum point of $d_{\text{eff,B}}$ is outside the plot region, but the important observation here is that $St_{\text{eff,B}}$ provides a theoretical maximum expression for the effective Stokes number.

efficiency's sensitivity to velocity changes. Because of the steep increase in η with increasing St in the range $0.20 < St < 0.40$, an adjustment to an effective Stokes number gives the highest difference in this region. Since u_{\max} is the maximum velocity a particle could possibly have, capture efficiencies for $St_{\text{eff},B}$ is expected to give a theoretical upper boundary of the turbulent capture efficiency. This is confirmed in the figure. Also, it is important to note that increased particle velocity in the effective Stokes number, i.e. $St_{\text{eff},B}$ compared to $St_{\text{eff},A}$, shifts the center of the peak in relative difference towards smaller Stokes numbers. This is due to that $St_{\text{eff},B}$ represents a larger shift in the Stokes number, thus a lower value of $St_{\text{eff},B}$ corresponds with the original Stokes number where η is steepest. This indicates that particles in the $k_n = 1.5$ turbulent flow are accelerated to higher velocities than in the $k_n = 5$ case, since the peak of the relative difference is shifted to the left, in addition to being larger.

The reason for increased turbulent capture efficiency is believed to be increased particle velocities. The particles accelerated streamwise will have a higher probability of deposition on the cylinder. Similarly, the particles accelerated anti-streamwise will have a lower probability of deposition. The turbulence will introduce particles with an interval of velocities in the vicinity of the cylinder, rather than particles with one distinct velocity, as in the laminar case. But why do we not see the same increased capture efficiency for the lowest Stokes numbers ($St < 0.15$)? As Haugen & Kragset argued, particles with sufficiently low Stokes numbers will follow the fluid flow perfectly. If the boundary layer of the cylinder is unchanged when turbulent inflow is introduced, the turbulence will not bring the smallest particles any closer to the cylinder. Perhaps more importantly, as was seen in figure 5.11, the capture efficiency's sensitivity to Stokes number is smaller in this range of Stokes numbers. Therefore, a small perturbation in particle velocity will not give a large difference in capture probability. The same applies for the larger particles, with $St > 0.5$, where the capture efficiency flattens with increasing Stokes numbers.

The small scale turbulence, with forcing at $k_n = 5$, did not produce as large differences as was seen in the large scale case. A possible explanation for this can be that the smaller eddies give smaller accelerations in all directions. This will result in fewer particles with an increased streamwise velocity. The spread of particle velocities will probably be more compact. But still, the differences seen between laminar inflow and $k_n = 5$ turbulent inflow, is believed to be from the same cause as for $k_n = 1.5$ turbulence. Small increases in streamwise velocity will help the particles penetrate the boundary layer.

The implementation of turbulence in 2D simulations in this project showed that somewhat similar results as from 3D can be expected. The previous argument that an increase in particle velocity is the main factor that increases the turbulent capture probability, does not indicate that 2D simulations are insufficient. Streamwise eddy accelerations can occur also in 2D. The challenge when finding turbulent capture efficiency in 2D, however, is to ensure that the turbulence is of a general character. In this project, where a 2D slice of a 3D turbulence snapshot is used as turbulent inflow, the limited variation in turbulent structures present is probably limiting the quality of the results.

5.7.1 Possible sources of error

The turbulence that was created by forcing, was forced with an amplitude giving u_{\max} corresponding to 60 – 80% of the mean flow, U_0 , in the cylinder domain. The reason for this choice was the desire to maximize the intensity of the turbulence without getting trouble with the NSCBC boundary conditions. When comparing the turbulence created by forcing at $k_n = 5$ and $k_n = 1.5$, we need to take into account that the larger eddies with wavenumber $k_n = 1.5$ contain more energy than the $k_n = 5$ eddies when u_{rms} is the same. The difference in total turbulent kinetic energy

$$\tilde{E}_{\text{tot}} = \int E(k)dk, \quad (5.3)$$

reflects this¹. For forcing at $k_n = 5$, the total turbulent kinetic energy is $\tilde{E}_{\text{tot},k5} = 68.5$ J/kg, while the energy for the other case is $\tilde{E}_{\text{tot},k1.5} = 73.3$ J/kg. This difference is small, however, compared to the large differences seen in capture efficiency of the two cases with turbulent inflow.

Possibly a more important factor explaining differences between $k_n = 5$ and $k_n = 1.5$ turbulence is the dissipative effect. Since the cylinder flow domain has no turbulent forcing, the turbulent energy will gradually decay. Because of the power being concentrated around a higher wavenumber, the $k_n = 5$ turbulence will be subject to a stronger decay, and thereby the turbulence is more suppressed.

5.7.2 Further issues

Comparison with the experimental results of Douglas & Ilias [14] showed that higher Reynolds numbers will probably give stronger turbulent effects on particle deposition. When conducting direct numerical simulations, however, there is always the limitation of the computational cost. The grid resolution requirements and running time dictates limitations on the Reynolds number in DNS. The present limitation on the boundary conditions, requiring non negative velocities at the inlet, set strict limitations on the maximum intensity of the turbulence used. If this could be resolved, an increased relative intensity of the turbulence, u_{rms}/U_0 , would probably give stronger effects on particle deposition. This way, the turbulent effects will be stronger, but without putting increasing demands on the grid resolution. Also, by increasing the turbulent intensity, the eddy stokes numbers will increase. This project has studied the mechanisms of turbulent particle deposition for eddy stokes numbers less than 1. To get an overall understanding of the subject, the full range of eddy stokes numbers should be investigated.

In many applications, especially in heat exchangers, there will be a temperature gradient close to the cylinder surface. This may implicate that thermophoresis will play an important role of the particle behaviour in the boundary layer. Further investigation of this effect for both laminar and turbulent inflow could give better understanding on the relative importance of depositions due to thermophoresis and due to inertial impaction.

¹The units here are confusing; $[E(k)] \neq \text{J/kg}$, since $E(k)$ is energy per wavenumber, but $[E(k)dk] = [\tilde{E}] = \text{J/kg}$

Conclusion

Particle deposition on a circular cylinder was studied numerically using DNS. Results for capture efficiencies for laminar inflow was compared with different cases of turbulent inflow. Turbulence was created by isotropic forcing in a presimulation. Two different scales of forcing were considered, $k_n = 1.5$ and $k_n = 5$. Particles were inserted and tracked in a Lagrangian formalism. Drag force from the fluid was used to calculate particle velocities. Particles impacting on the cylinder were recorded and removed from the simulation. The Reynolds number of the cylinder flow, Re , was 420.

The turbulent inflow increased the capture efficiency substantially for particles with Stokes numbers $0.15 < St < 0.4$. Variations in particle velocities was showed to be an important factor. Particles that are accelerated streamwise by the turbulent structures increase their inertia and thus the probability to penetrate the boundary layer of the cylinder. No indication of a change in the nature of the boundary layer was seen. An effective Stokes number where particle velocity changes are taken into account, have been suggested. The effective Stokes number relates the increased capture efficiencies for turbulent inflow to the original Stokes number for laminar inflow. In the range of Stokes numbers observed, $0.07 < St < 10.0$, the capture efficiency is monotonically increasing with increasing Stokes numbers. However, the sensitivity (steepness) of the capture efficiency to the Stokes number is highest in the boundary stopping range $0.2 < St < 0.5$. Therefore, it is in this range that the turbulent velocity changes play the most important role on depositions. The large scale turbulence, characterized by forcing at $k_n = 1.5$, produced significantly higher capture efficiencies than the $k_n = 5$ turbulence. The higher relative decay of the $k_n = 5$ turbulence can partly explain this. The eddy Stokes number, $St_{\text{eddy}} = \tau_p / \tau_{\text{eddy}}$, was below unity for all Stokes numbers studied, indicating that all particles would easily interact with the turbulent structures. High intensity effects from $St_{\text{eddy}} \geq 1$ was not investigated.

All results from turbulent inflow were produced from 3D simulations. For laminar inflow, 2D simulations were proved to be sufficient. In addition, 2D simulations with turbulent inflow were conducted. Turbulent capture efficiencies from 2D and 3D simulations showed a somewhat similar behaviour. Although the implementation of turbulence in 2D was relatively simple, it can be concluded that simplifying the simulations to two dimensions can be useful for qualitative observations.

Appendix A

Parameters used in the Pencil Code

Dimensional values used as input to the Pencil Code are represented here:

Size of domain, presimulation [m]	$0.2 \times 0.2 \times 0.2$
Size of domain, main simulation [m]	$0.4 \times 0.2 \times 0.2$
Coordinates of domain [m]	$x : 0.0 \rightarrow 0.4$, $y : -0.1 \rightarrow 0.1$, $z : -0.1 \rightarrow 0.1$
Cylinder center position, (x, y) [m]	$(0.2, 0.0)$
Cylinder diameter	$d_c = 0.0337$ m
Mean flow velocity	$U_0 = 5$ m/s
Kinematic viscosity for $Re_c = 420$	$\nu = 4 \cdot 10^{-4}$ m ² /s
Speed of sound, presimulation	$c = 20$ m/s
Speed of sound, main simulation	$c = 40$ m/s
Mass density, particles	$\rho_p = 1000$ kg/m ³

Bibliography

- [1] Pope S. B. *Turbulent Flows*. Cambridge University Press, 2000.
- [2] Crowe C., Sommerfeld M., and Tsuji Y. *Multiphase flows with droplets and particles*. CRC Press LLC, 1998.
- [3] Wang H. C. Theoretical adhesion efficiency for particles impacting a cylinder at high reynolds number. *Journal of Aerosol Science*, 17:827–37, 1986.
- [4] Davies C.N. Definitive equations for the fluid resistance of spheres. *The proceedings of the physical society*, 57(322), 1945.
- [5] Ranz W. E. and Wong J. B. Impaction of dust and smoke particles on surface and body collectors. *Industrial & Engineering Chemistry Research*, 44:1371–81, 1952.
- [6] Rosner D. E. and Tandon P. Rational prediction of inertially induced particle deposition rates for a cylindrical target in a dust-laden stream. *Chemical Engineering Science*, 50:3409–31, 1995.
- [7] Kasper G., Schollmeier S., Meyer J., and Hoferer J. The collection efficiency of a particle-loaded single fiber. *Journal of Aerosol Science*, 40:993–1009, 2009.
- [8] Lodato G., Domingo P., and Vervisch L. Three dimensional boundary conditions for direct and large-eddy simulation of compressible viscous flows. *Journal of Computational Physics*, 227:5105–43, 2008.
- [9] Saddoughi S. G. and Veeravalli S. V. Local isotropy in turbulent boundary layers at high reynolds number. *J. Fluid Mech*, 268:333–72, 1994.
- [10] Zhou H., Jensen P.A., and Frandsen F.J. Dynamic mechanistic model of superheater deposit growth and shedding in a biomass fired grate boiler. *Fuel*, 86:1519–33, 2007.
- [11] Kim J., Moin P., and Moser R. Turbulence statistics in fully developed channel flow at low reynolds number. *J. Fluid Mech*, 177:133–66, 1987.
- [12] Poinso T. J. and Lele S. K. Boundary conditions for direct simulations of compressible viscous flows. *Journal of Computational Physics*, 101:104–29, 1992.

- [13] Williamson C. H. K. Vortex dynamics in the cylinder wake. *Annu. Rev. Fluid Mech.*, 28:477–539, 1996.
- [14] Douglas P. L. and Ilias S. On the deposition of aerosol particles on cylinders in turbulent cross flow. *Journal of Aerosol Science*, 19:451–62, 1988.
- [15] Haugen N. E. L. and Kragset S. Particle impaction on a cylinder in a cross flow as function of stokes and reynolds numbers. *submitted J. Fluid Mech.*, 2010. In press.
- [16] Chertkov M., Connaughton C., Kolokolov I., and Lebedev V. Growing condensate in two-dimensional turbulence. *submitted Phys. Rev. Lett.*, 2007. Unpublished.
- [17] Lesieur M. *Turbulence in Fluids*. Dordrecht: Springer, 2008.
- [18] Davies C. N. and Peetz C. V. Impingement of particles on a transverse cylinder. *Proceedings of the Royal Society of London. Series A, Mathematical and Physical Sciences*, 234:269–95, 1955.
- [19] Moin P. and Mahesh K. Direct numerical simulation: A tool in turbulence research. *Annu. Rev. Fluid Mech.*, 30:539–78, 1998.
- [20] Fan J. R., Zhou D. D., and Cen K. F. Numerical simulation of tube erosion by particle impaction. *Wear*, 142(1):171–84, 1991.
- [21] Pearson B. R., Yousef T. A., Haugen N. E. L., Brandenburg A., and Krogstad P. Å. Delayed correlation between turbulent energy injection and dissipation. *Physical Review E*, 70, 2004.
- [22] Srikanth S., Das S. K., Ravikumar B., Rao D. S., Nandakumar N., and Vijayan P. Nature of fireside deposits in a bagasse and groundnut shell fired 20mw thermal boiler. *Biomass & Bioenergy*, 27:375–84, 2004.
- [23] Dobler W. and Brandenburg A. *The Pencil Code: A High-Order MPI code for MHD turbulence*. <http://www.nordita.org/software/pencil-code/doc/manual.pdf>.
- [24] Dobler W., Haugen N. E. L., Yousef T. A., and Brandenburg A. Bottleneck effect in three-dimensional turbulence simulation. *Physical Review E*, 68, 2003.
- [25] Muhr W. *Theoretical and Experimental Investigation of Particle Deposition in Fibrous Filters by Field and Inertial Forces*. PhD thesis, Universität Karlsruhe, 1976.
- [26] Kaneda Y., Ishihara T., Yokokawa M., Itakura K., and Uno A. Energy dissipation rate and energy spectrum in high resolution direct numerical simulations of turbulence in a periodic box. *Physics of Fluids*, 15, 2003.
- [27] Li Z. and Wang H. Drag force, diffusion coefficient, and electric mobility of small particles. i. theory applicable to the free-molecule regime. *Physical Review E*, 68(061206), 2003.